geosciences

Article

Late Cretaceous through Cenozoic Paleoenvironmental History of the Bagua Basin, Peru: Paleoelevation Comparisons with the Central Andean Plateau

Federico Moreno [1,2,*], Carmala N. Garzione [1,3], Sarah W. M. George [2], Lauren Williams [1,4], Fabiana Richter [1,5] and Alice Bandeian [1]

1 Earth and Environmental Sciences Department, University of Rochester, Rochester, NY 14611, USA; garzione@arizona.edu (C.N.G.); lauren.a.williams3201@gmail.com (L.W.); fabi.richter@gmail.com (F.R.); alicebandeian417@gmail.com (A.B.)
2 Department of Geosciences, University of Arizona, Tucson, AZ 85721, USA; swmgeorge@arizona.edu
3 College of Sciences, University of Arizona, Tucson, AZ 85721, USA
4 Geology and Mineral Resources, Virginia Department of Energy, Charlottesville, VA 22903, USA
5 Laboratório de Estudos Geodinâmicos, Geocronológicos e Ambientais, Institute of Geosciences, University of Brasília, Brasilia 70910-900, DF, Brazil
* Correspondence: federicomrn@gmail.com

Abstract: Located in northern Peru, at the lowest segment of the Central Andes, the Bagua Basin contains a Campanian to Pleistocene sedimentary record that archives the local paleoenvironmental and tectonic history. We present new $\delta^{18}O$ and $\delta^{13}C$ signatures of pedogenic carbonate nodules from paleosols in the Campanian–Maastrichtian Fundo El Triunfo Formation and in the upper Eocene–middle Miocene Sambimera Formation to reconstruct the isotopic composition of paleo-meteoric water and the floristic biome. We compare these results to modern isotopic values from a newly obtained modern water transect to interpret the environmental evolution of this area and its relationship with the neighboring Eastern Cordillera. A ~2‰ $\delta^{18}O$ depletion between the latest Cretaceous and the latest Eocene reflects a shift from a coastal to inland environment. A negative $\delta^{18}O$ shift of ~3‰ from the middle Miocene to the present day reveals the establishment of the Eastern Cordillera as an orographic barrier for the moisture traveling westward, sometime after deposition of the top of the Sambimera Formation at ~13 Ma. A shift in the $\delta^{13}C$ signature from ~−25‰ in the Campanian–Miocene deposits to ~−23‰ in modern–Holocene times suggests a change in biome from dominant C3 plants to a mixture of C3 and C4 plants. This environmental shift reflects both the late Miocene global C4 expansion and the transition to more arid conditions in the basin. The Campanian–middle Miocene environmental reconstruction of the Bagua Basin indicates a steady paleoelevation setting in the northernmost Central Andes during most of the Cenozoic and constrains the uplift of the Eastern Cordillera to the late Miocene–Pleistocene. This paleoelevation history contrasts with that of the Central Andean Plateau, which is characterized by two major episodes of surface uplift: early–middle Miocene and late Miocene–Pliocene. The contrasting modern topographic configuration of the Central Andean Plateau and the northernmost Central Andes gives rise to the question of what factors created such a dramatic difference in topographic evolution of the two regions that shared an overall common tectonic history. We discuss the possible factors responsible for this contrasting topographic configuration and suggest that the diachronous flat slab episodes are likely a major factor, resulting in greater shortening and crustal thickness and, ultimately, in earlier surface uplift episodes occurring in the Central Andean Plateau.

Keywords: northern Central Andes; Bagua Basin; oxygen and carbon stable isotopes; paleoelevation history

Citation: Moreno, F.; Garzione, C.N.; George, S.W.M.; Williams, L.; Richter, F.; Bandeian, A. Late Cretaceous through Cenozoic Paleoenvironmental History of the Bagua Basin, Peru: Paleoelevation Comparisons with the Central Andean Plateau. *Geosciences* **2022**, *12*, 242. https://doi.org/10.3390/geosciences12060242

Academic Editors: Lev Eppelbaum and Jesus Martinez-Frias

Received: 14 February 2022
Accepted: 30 May 2022
Published: 10 June 2022

1. Introduction

The northernmost termination of the Central Andes in northern Peru and southern Ecuador shares a similar latest Cretaceous through Cenozoic tectonic history with the rest of the Central Andes, yet their peak and mean surface topography sit at considerably lower elevations (Figure 1). The contrasting topographic expression between two segments of the Central Andes that share a similar tectonic history may be explained by a number of variables that control the magnitudes of shortening and magmatic addition. These variables include subduction angle, plate convergence velocity, precipitation, and erosional regimes [1–4]. To understand how the interplay of these factors impacts the geodynamic mechanisms that govern such contrasting topographic expressions, it is critical to constrain the elevation history of the northernmost Central Andes and compare it with that of the well-studied Central Andean Plateau, which has been extensively studied in the last few decades [5,6].

The tectonic history of the Central Andes has been studied at different latitudes through a number of techniques, including basin analysis, thermochronology, structural geology, and stable isotopes [5–12]. Episodes of shortening coupled with orogenic loading and flexural subsidence occurred roughly synchronously along the latitudinal extent of the Central Andes. Initial shortening and orogenic loading during the latest Cretaceous to earliest Cenozoic have been documented in the southern, central, and northern Central Andes [11–19]. Eocene to middle Miocene eastward advance of the deformation front resulted in the onset of shortening in the Eastern Cordillera at the latitudes of the Central Andean Plateau [9,12,20–23], as well as in increased shortening in the Western Cordillera of the northern Central Andes [7,8,11,13,24,25]. Finally, during the late Miocene to Pliocene a new orogenic episode caused deformation to propagate into the Subandean zone adjacent to Central Andean Plateau [9,26–28] and the onset of the deformation of the Eastern Cordillera and, subsequently, of the Subandean zone, in the northern Central Andes [7,8,11,13,24,25,29].

Stable isotopes, paleobotanical, and phylogenetic studies in the southern Central Andes, at the latitudes of the Central Andean Plateau, reveal punctuated changes in elevation during the middle Miocene to Pliocene. Two major uplift pulses contributed to the modern topographic configuration of the Central Andean Plateau [5]. An initial phase during the early to middle Miocene resulted in ~3–4 km of uplift in the Western and Eastern cordilleras [6,30–32]. The second major pulse took place in the late Miocene–Pliocene and was responsible for further uplift of the Western and Eastern cordilleras and for the rise of Altiplano province to its modern elevation [32–37]. In contrast, little is known about the elevation history of the relatively low northern Central Andes.

Nested between the Western and Eastern cordilleras, in the northernmost segment of the Central Andes, the intermontane Bagua Basin contains the sedimentary record of the Late Cretaceous and Cenozoic growth of the mountain belt [25]. This paper presents oxygen and carbon stable isotope data from Upper Cretaceous and Cenozoic pedogenetic carbonate nodules from sedimentary units of the Bagua Basin to reconstruct paleo-meteoric water and paleo-flora compositions. Paleoclimate and paleoecological reconstructions are compared with the modern isotopic fingerprint of the basin, to investigate the elevation history of this atypical low elevated portion of the Andes. We look for a negative shift in the isotopic composition of paleo-meteoric water associated with the onset of the rain-shadow effect exerted by the growth of the Eastern Cordillera. Additionally, we explore how different factors influencing tectonic shortening rates might have played a role in shaping the contrasting topographic expressions of the northernmost termination of the Central Andes and the Central Andean Plateau.

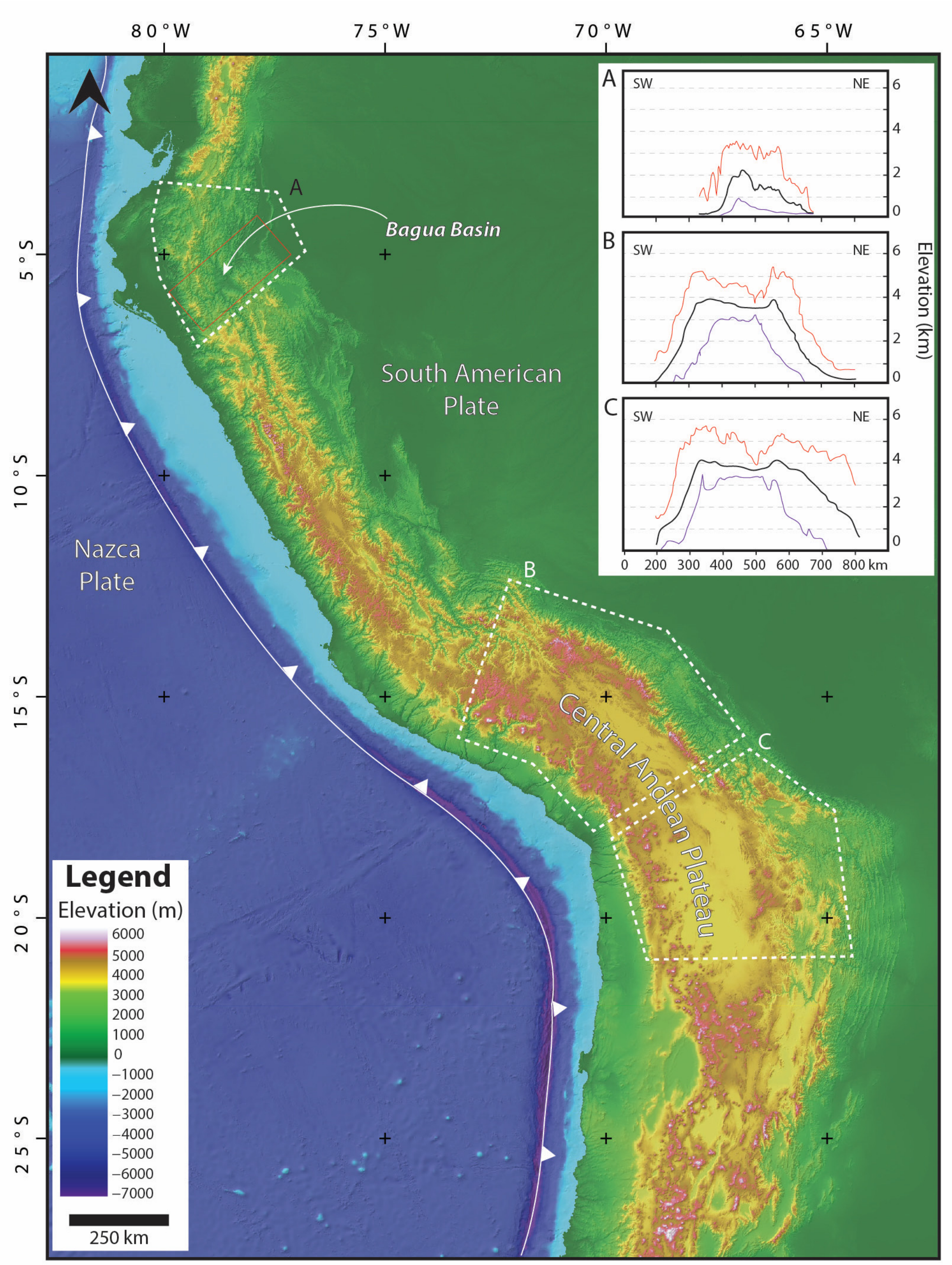

Figure 1. Digital elevation model of the Central Andes showing the location of the Bagua Basin and the Central Andean Plateau. Polygons and swath topographic profiles highlight the contrasting morphology of the (**A**) northernmost Central Andes and (**B**,**C**) the Central Andean Plateau domains. Black line in the swath topographic profiles shows the mean elevation, and orange and purple lines show maximum and minimum elevation, respectively. Swath topographic profiles were constructed using the online tool to produce swath topographic profiles along curved geomorphic features by Hergarten, et al. (2014) [38]. Red square shows the location of Figure 6A.

2. Background

2.1. Geological Setting

The Central Andes extends from ~3° S to ~33° S along the western margin of the South American plate with a mean elevation of ~2500 m and mean maximum elevation of ~5000 m. The northern termination, between ~3° S and ~7° S, is atypically low with an average elevation of ~1000 m (Figure 1). There, the Bagua Basin sits at a mean elevation of 500 m and is flanked by the Eastern and Western cordilleras. At these latitudes the highest peaks of the Western and Eastern cordilleras barely reach 4000 m [39]. The Western Cordillera is composed of the Cretaceous to Cenozoic magmatic arcs, which intruded Paleozoic and Mesozoic metamorphic and sedimentary rocks that were folded and faulted in the Marañon Fold-Thrust Belt during early Andean orogenesis [8,13]. The Eastern Cordillera is composed of blocks of Paleozoic through Cenozoic rocks uplifted as a result of the inversion of the Permo-Triassic extensional system since the middle Miocene [11,25,40].

In the latest Cretaceous, the tectonic regime in the northernmost Central Andes shifted from dominantly extensional to contractional, resulting in the onset of the Andean orogeny [11]. Three Late Cretaceous–Cenozoic orogenic episodes have been documented in this region [13,41]. An initial pulse of shortening during the latest Cretaceous is characterized by the onset of deformation in the Marañon Fold-Thrust Belt in the Western Cordillera. A second orogenic episode during the Eocene–middle Miocene resulted in the eastward propagation of the deformation front, causing further deformation in the Marañon Fold-Thrust Belt and ultimately capturing the Bagua Basin. A final orogenic episode during the late Miocene–Pliocene was characterized by further migration of the deformation front to the east, causing the inversion of the extensional Permo-Triassic system, resulting in initial deformation of the Eastern Cordillera and subsequent thin skin deformation on the Subandean zone [7,8,11,13,25] (Figure 2).

2.2. Climate and Ecology

The modern climate of the Bagua Basin is hot and dry with marked rainfall seasonality. High and low average temperatures are 32 °C and 20 °C, respectively, while precipitation is ~800 mm/year with most of the rainfall occurring during the wet season October–May [42–44]. Tropical dry forest is the prevailing biome in the landscape of the basin [45–47]. This precipitation regime and biome composition contrasts with that of the eastern slope of the Eastern Cordillera at the same latitude and altitude (Figure 3). There, the climate is characterized by temperatures and rainfall seasonality similar to that of the Bagua Basin, while precipitation is ~3000 mm/year [42–44], and the biome composition is dominated by tropical moist forest [45–47]. These contrasting climatic and ecological conditions are the result of the rain-shadow effect exerted by the Eastern Cordillera that serves as a barrier for the low-level warm and moist trade winds travelling from the east, thereby causing its adiabatic cooling and subsequent precipitation on the eastern slope of the orogen [42,48,49]. The moisture that precipitates in this region originates in the Atlantic Ocean, is transported to the west by the trade winds that converge in the Intertropical Convergence Zone [50], and it is largely affected by the evapotranspiration of vegetation during its ~4000 km traverse over the Amazon forest [51].

2.3. Basin Evolution and Stratigraphy

The Bagua Basin contains a protracted sedimentary record of the Late Cretaceous and Cenozoic tectonic history of the northernmost Central Andes [25]. Onset of shortening in the latest Cretaceous resulted in the development of a foreland basin as a response to the tectonic load of the nascent orogen. Deposits related to this shortening event are chronicled in the middle Campanian–Maastrichtian Fundo El Triunfo Formation, which contains the distal foredeep sedimentary deposits of a meandering fluvial system. Sedimentation in the distal foredeep continued during the Paleocene–earliest Eocene with the braided fluvial deposits of the Rentema Formation. During the Eocene–middle Miocene, the deformation front advanced eastward, causing a progressive increase in subsidence rates in the Bagua Basin. The Eocene Cajaruro Formation was deposited in a fluvio-lacustrine system in a middle foredeep setting, and the upper Eocene–Oligocene lower Sambimera Formation represents a meandering fluvial system in a proximal foredeep setting. The deformation front continued to migrate to the east, capturing the Bagua Basin in the middle Miocene. At that time, the upper Sambimera Formation was deposited in a wedge top setting. An erosive boundary separates the Sambimera Formation from the San Antonio Formation.

This boundary records the final transit of the deformation front eastward of the basin. The upper Miocene–Pliocene San Antonio Formation contains the deposits of a fluvio-lacustrine system active in an intermontane setting that resulted from the initial uplift of the Eastern Cordillera. The Pleistocene conglomerates of the Tamborapa Formation and Holocene sandy and gravely deposits, cap the sedimentary succession. Details of the Campanian–Pliocene evolution of the foreland Bagua Basin are discussed in Moreno, et al. (2020) [25].

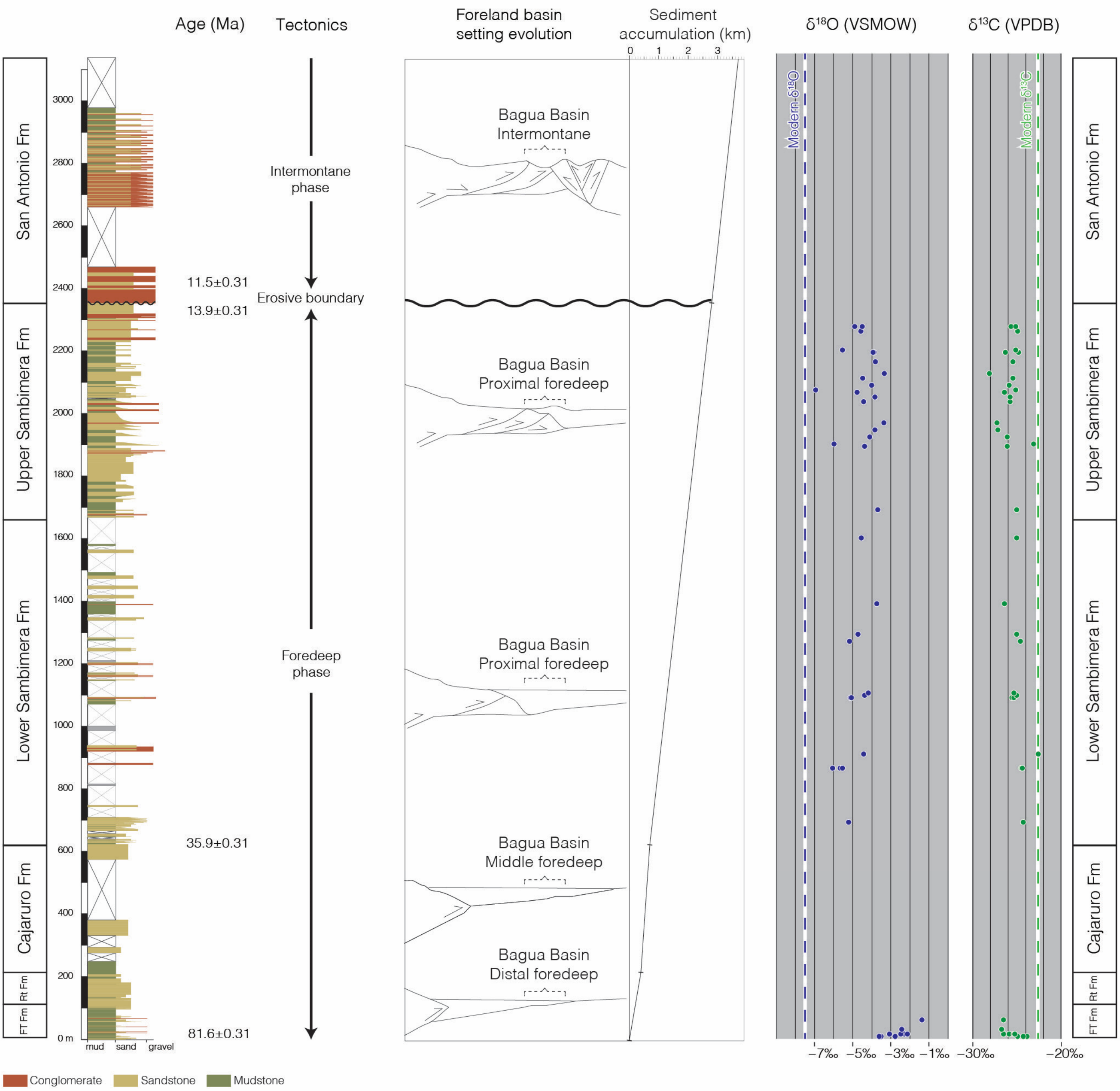

Figure 2. Generalized stratigraphic section of the Campanian to Pliocene sedimentary succession in Bagua Basin. Age constraints are maximum depositional ages from zircon U-Pb geochrononology from Moreno, et al. (2020) [25]. Panels in the left shown from left to right, tectonic and foreland basin setting, historical de-compacted sediment accumulation curve [25], and $\delta^{18}O_{mw}$ and $\delta^{13}C_o$ results for the Fundo El Triunfo and Sambimera formations. Blue and green dashed vertical lines indicate the average modern signature for $\delta^{18}O_{mw}$ and $\delta^{13}C_o$ calculated as the arithmetic mean of the $\delta^{18}O$ values of the water samples collected in the Bagua Basin and of the $\delta^{13}C$ of the plants collected in the Bagua Basin respectively. Analytical errors (1 sigma) are smaller than ±0.1 for $\delta^{18}O$ and smaller than ±0.06 for $\delta^{13}C$. Abbreviations: FT Fm = Funfo El Triunfo Formation; Rt Fm = Rentema Formation.

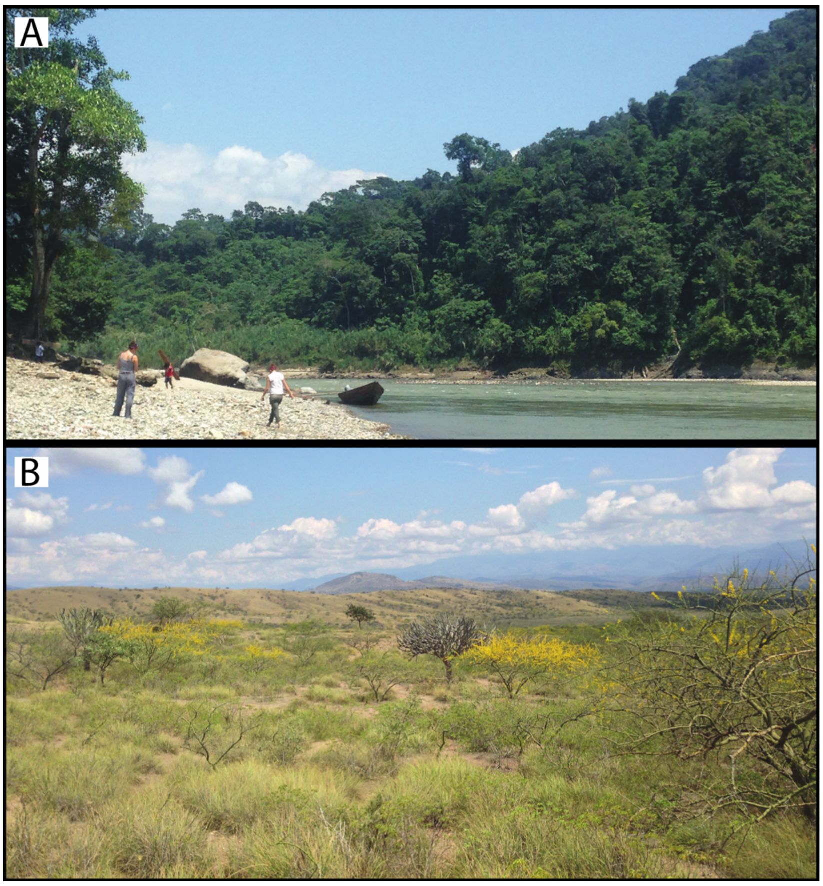

Figure 3. Photographs showing the contrasting landscape between (**A**) the eastern slope of the Eastern Cordillera and the (**B**) Bagua Basin at the same latitude.

Paleosols in the Bagua Basin

Paleosols occur in the middle Campanian–Maastrichtian Fundo El Triunfo Formation and in the upper Eocene–middle Miocene Sambimera Formation. In the Fundo El Triunfo Formation, paleosols occur in the upper part of the up-to-20-m-thick bodies of stacked mudstone beds that represent flood plain deposits. The paleosols are red, massive, fine grained, and contain root traces in their upper part. Toward the base their color fades to mottled purple-grey, and the grain size is coarser. Pedogenic carbonate nodules are incipient, reaching a few millimeters in size, and occurring at ~70–100 cm from the top of the paleosol (Figure 4).

Paleosols in the Sambimera Formation occur throughout the thickness of the unit (~1600 m) in floodplain intervals. Paleosols show strong color and texture change across the pedogenic profile from red, clay-sized and massive at the top, fading to light red to light grey mottled in the middle part, and to light grey with coarser grain (silt to sand) and crude laminations at the base. They preserve root traces in the upper part, and pedogenic carbonate nodules toward the middle part between ~70 cm and 1.5 m from the top. The size of carbonate nodules varies from millimeters up to a few centimeters for well-developed nodules (Figure 4).

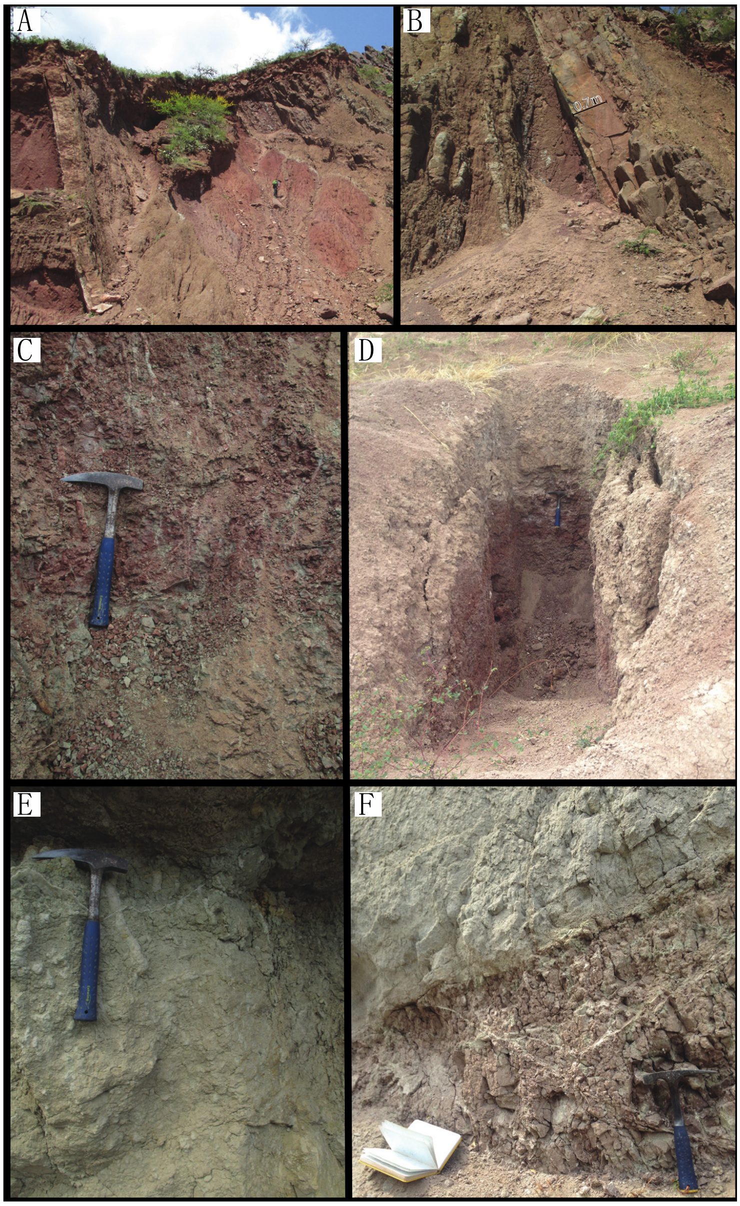

Figure 4. Paleosols photographs from the Fundo El Triunfo Formation (**A**,**B**) and the Sambimera Formation (**C**–**F**).

3. Materials and Methods

As rain-out occurs, the oxygen isotopic composition of water in air masses evolves following Rayleigh distillation where the heavy oxygen (^{18}O) is preferentially removed from the air mass and the light oxygen (^{16}O) is retained [52]. Other factors including evapotranspiration and mixing of air masses can influence the oxygen isotopic composition of water in the air mass [53]. In the modern northern Central Andes, precipitation is derived from water vapor originating in the Atlantic Ocean and transported westward by the trade winds that converge in the intertropical convergence zone, with minimal air mass mixing over this atmospheric pathway [49,54–56]. On the other hand, recycling of enriched precipitation via evapotranspiration along the transit over the Amazon Forest affects the oxygen isotopic composition of the water vapor by reducing the net depletion of ^{18}O [51,53,57]. Modern data and models suggest a total depletion of the oxygen isotopic composition of atmospheric water vapor of only ~3.5‰ during its ~4000 km long travel past the Amazon Forest [46]. In western tropical South America, larger changes in the oxygen isotopic composition of the vapor mass occur when the air mass reaches the Andes.

As the airmass ascends over the Andes, it cools through adiabatic expansion, resulting in condensation and precipitation [51,58,59]. In this manner, the rain-shadow effect exerted by the Andes is reflected in the oxygen isotopic composition of the meteoric water on the windward and leeward sides of the orogen [50,51,59]. The oxygen isotopic composition of meteoric water can be archived in authigenic and biogenic minerals. If these minerals are preserved in the sedimentary record and are not subjected to deep burial diagenesis, then past environmental conditions can be reconstructed [33,60–62].

The isotopic composition of carbon in terrestrial environments is dominantly determined by the ratio of C3 to C4 plants in the landscape [63]. C3 and C4 use different photosynthetic pathways, which is ultimately reflected in their carbon isotopic composition. C3 plants are mostly trees and shrubs and have a carbon isotopic composition between −22‰ and −32‰, with an average of −27‰. C4 plants are mostly grasses and have an isotopic signature between −10‰ and −15‰ with an average of −12‰. C4 plants appeared in the geological record in the early Miocene [64], but only expanded globally around 8 to 6 Ma. C4 plants are well-adapted to climates with dry conditions and/or low atmospheric CO_2 concentrations [63,65–69].

Pedogenic carbonate nodules are formed in climates with seasonal precipitation and are produced by the interaction of the soil-respired carbon dioxide (CO_2), meteoric water (H_2O), and free calcium cations (Ca^+) in the soil. Soil CO_2, produced by plant respiration and the break-down of organic matter in the soil, is converted to bicarbonate (HCO_3^-) through interaction with meteoric water (H_2O). During the dry season, water loss through evaporation and plant root absorption drives calcium carbonate ($CaCO_3$) precipitation in the soil. Because calcium carbonate uses the meteoric water and the soil-respired CO_2 to precipitate, it preserves the isotopic composition of oxygen from meteoric water ($\delta^{18}O$) and of carbon from respired soil carbon dioxide ($\delta^{13}C$) and can therefore be used to assess past environmental and ecological conditions [33,63,70,71].

To reconstruct the oxygen isotopic composition of meteoric water archived in pedogenic carbonates, the fractionation between soil water and pedogenic calcite has to be taken in account. This relationship is affected by seasonality and is temperature dependent. In climates with strong seasonality, the oxygen isotopic composition of calcite may be biased to more positive values given that mineral precipitation takes place as the soil is drying out. To minimize the evaporation artifact, pedogenic carbonates were sampled as deep as possible in the soil profile, at a minimum depth of 60 cm below the top of the paleosol. The relation between the water–calcite fractionation and temperature have been empirically established by Kim and O'Neil (1997) [72] in the equation:

$$1000 \times \ln \alpha_{\mathrm{Calcite-H_2O}} = 18.03\left(10^3 \times \mathrm{T}^{-1}\right) - 32.42 \tag{1}$$

where α is the fractionation factor between calcite and water, and T is the temperature of fractionation in degrees Kelvin. Assuming soil temperature, we use this equation to reconstruct the $\delta^{18}O$ values of meteoric water that infiltrated the soil. Similarly, to reconstruct the isotopic composition of plants growing in the soil, it is necessary to account for the fractionation between soil-respired CO_2 and pedogenic calcite. This fractionation is temperature dependent based on the equation:

$$1000 \times \ln \alpha_{\mathrm{CO_2-H_2O}} = -2.4612 + \left(7.6663 \times 10^3 \times \mathrm{T}^{-1}\right) - \left(2.9880 \times 10^6 \times \mathrm{T}^{-2}\right) \tag{2}$$

where α is the fractionation factor between calcite and water, and T is the temperature of fractionation in degrees Kelvin [73]. Additionally, an enrichment of 4.4‰ due to CO_2 diffusion in the soil has to be accounted for [63]. We assumed a temperature of 30 °C for calcite precipitation based on clumped isotope temperatures achieved for carbonate precipitation in Miocene deposits of southern Peru [36]. According to equations (1) and (2) above and using 30 °C for the calcite precipitation temperature, the enrichment factor between the $\delta^{18}O$ of meteoric water ($\delta^{18}O_{mw}$) and pedogenic calcite ($\delta^{18}O_{pc}$) is ~−27.1‰, and between the $\delta^{13}C$ of soil-respired CO_2 ($\delta^{13}C_o$) and pedogenic calcite ($\delta^{13}C_{pc}$) is ~−9.7‰ plus ~−4.4‰ due to diffusion (total fractionation = −14.1%).

Paleosols were identified in the field on the base of sedimentological features, such as grain size and color change with depth, root traces, mottling, and presence of pedogenic carbonate nodules. Pedogenic carbonate nodules were sampled at ~60 cm below the top of the paleosol to minimize evaporation bias on the $\delta^{18}O_{mw}$ value and the effects of diffusion of atmospheric CO_2 on the $\delta^{13}C_{pc}$ value.

To achieve the modern isotopic signature of meteoric water and vegetation in the Bagua Basin, water from small creeks, rainfall, and the dominant vegetation were sampled. Additionally, pedogenic carbonate nodules from one modern-Holocene soil (Figure 5) and the calcareous shell of two large modern terrestrial snails were collected. Meteoric water samples were taken from creeks in a longitudinal transect including the Western Cordillera, the Bagua Basin, and the Eastern Cordillera. Creeks with small catchment areas close to their headwaters were preferentially sampled to minimize the catchment size and elevation range of source waters. Additionally, one sample from rainfall in the basin was analyzed. Modern vegetation samples were collected from 10 of the most common shrubs and grasses in the Bagua Basin to obtain the carbon isotopic signature of the prevailing flora.

Figure 5. Modern Holocene deposits from where pedogenic carbonates were collected and analyzed to achieve the modern isotopic fingerprint of meteoric water and soil-respired CO_2 in the Bagua Basin. White star shows where the pedogenic carbonates were sampled.

Samples were prepared and analyzed at the SIREAL (Stable Isotope Ratios in the Environment Analytical Laboratory) at the University of Rochester. Isotopic results for oxygen and carbon are reported with respect to VSMOW (Vienna Standard Mean Ocean Water) and VPDB (Vienna Pee Dee Belemnite) respectively.

Pedogenic carbonate nodules and calcareous shells were crushed to powder using a manual porcelain mortar and then pretreated with 30% oxygen peroxide to avoid organic carbon traces. The $\delta^{18}O_{pc}$ and $\delta^{13}C_{pc}$ were measured from CO_2 that evolved from carbonate samples during reaction with 103% H_3PO_4. The $\delta^{18}O$ and $\delta^{13}C$ analyses were carried out using a Finnigan Delta plus XP CF-IRMS in continuous flow mode coupled with a Gas Bench II peripheral device (both manufactured by Thermo Fisher Scientific, Waltham, MA, USA) and ratio determinations were based on the analysis of internal crayola, prang, and thermo chalk standards within the analytical session. SIREAL internal standards are calibrated using international standards, NBS−18, NBS−19, and L-SVEC.

Plant leaves were dried in an oven at 60 °C for 24 h, pulverized using a Wig-L-Bug grinder, combusted at 980 °C using a Zero Blank Autosampler and an Elemental Combustion System 4010 Elemental Analyzer (both manufactured Costech, Milan, Italy), and analyzed on the Finnigan Delta plus XP CF-IRMS in continuous-flow mode. Results were normalized using three internal laboratory standards, SRM 8539, SRM 8542, and SRM 8541.

Water samples were analyzed using a Liquid Water Isotope Analyzer 24d (manufactured by Los Gatos Research, Mountain View, CA, USA). with a GC-PAL autosampler (manufactured by PAL, Zwingen, Switzerland). Analyses were normalized using two inhouse standards, calibrated to Vienna Standard Mean Ocean Water (VSMOW) and Vienna Standard Light Antarctic Precipitation (VSLAP).

4. Results

4.1. Modern $\delta^{18}O$ and $\delta^{13}C$

The $\delta^{18}O_{mw}$ values from rivers and creeks vary from ~−6.3‰ in the Subandean zone and eastern slope of the Eastern Cordillera, to ~−7.6‰ in the Bagua Basin, and ~−9‰ along the eastern slope of the Western Cordillera. Hydrogen isotopic compositions from these samples follow a similar trend, with average values of ~−38‰ in the Subandean zone and eastern slope of the Eastern Cordillera, ~−50‰ in the Bagua Basin, and ~−60‰ along the eastern slope of the Western Cordillera (Table 1).

Table 1. $\delta^{18}O_{mw}$ and δD_{mw} values for sample streams and rivers.

Location	ID	Latitude	Longitude	Elevation	δD_{mw}‰ (VSMOW)	$\delta^{18}O_{mw}$‰ (VSMOW)
Eastern Cordillera	14BB01w	−5.2945	−78.3909	708	−42.8	−7.0
	14BB02w	−5.2956	−78.3807	677	−41.3	−6.9
	14BB03w	−5.2956	−78.3807	677	−44.9	−7.3
	14BB04w	−5.2905	−78.3840	727	−38.8	−6.8
	14BB05w	−5.3045	−78.4278	338	−40.6	−6.8
	14BB06w	−5.3628	−78.4513	345	−39.7	−6.7
	14BB07w	−5.4028	−78.4486	358	−40.1	−6.2
	14BB09w	−5.4279	−78.4550	341	−44.4	−7.0
	16BG60w	−5.2990	−78.4247	375	−39.9	−6.1
	16BG61w	−5.2836	−78.3865	795	−39.3	−6.4
	16BG64w	−5.3931	−78.4496	354	−37.0	−6.6
	FM1601	−4.7467	−78.1237	253	−33.1	−5.9
	FM1602	−4.9802	−78.2273	441	−18.5	−4.0
	FM1603	−4.6114	−77.7141	211	−29.0	−4.9
	FM1604	−5.2406	−78.3611	368	−33.5	−5.7
	FM1605	−5.2808	−78.3761	840	−38.6	−6.6
	14BB08w [1]	−5.4078	−78.4531	335	−72.9	−10.4
Bagua Basin	14BB10w	−5.4690	−78.5119	398	−54.5	−8.5
	14BB11w	−5.5604	−78.6861	441	−49.0	−7.4
	16BG42w	−5.7253	−78.3147	855	−49.8	−7.7
	16BG43w	−5.7253	−78.3147	855	−46.5	−7.1
	16BG45w	−5.7207	−78.2739	1012	−54.6	−8.2
	16BG46w	−5.7277	−78.3451	697	−50.1	−8.2
	16BG49w	−5.6041	−78.4208	998	−48.8	−7.3
	16BG50w	−5.6030	−78.3987	1500	−52.6	−8.0
	16BG52w	−5.6071	−78.4422	767	−45.5	−7.2
	16BG59w	−5.7777	−78.3934	471	−44.8	−6.2
	16BG67w [2]	−5.6363	−78.5298	434	9.0	−1.1
Western Cordillera	14BB12w	−5.8870	−78.8277	565	−61.6	−8.9
	14BB13w	−6.0102	−78.8586	659	−60.0	−8.8
	14BB14w	−6.0205	−79.0055	811	−59.8	−9.0
	14BB15w	−6.0066	−79.1643	934	−59.5	−9.0
	14BB16w	−5.9517	−79.2310	1007	−64.1	−9.4
	14BB17w	−5.8000	−79.3739	1194	−65.9	−9.7
	14BB18w	−5.7867	−79.4279	1302	−50.4	−7.0

[1] sample collected from the Marañon River; [2] sample collected from rainfall.

The $\delta^{18}O_{pc}$ value recovered from pedogenic carbonates from a modern soil is −5.5‰; $\delta^{18}O_{mw}$ value reconstructed from these carbonates is −3.2‰ (Figure 5 and Table 2). Similarly, the $\delta^{18}O$ values obtained from two ~10-cm-long modern snail shells collected in the basin yielded bulk values of −4.2‰; the $\delta^{18}O_{mw}$ value reconstructed from these shells is −1.9‰ (Table 2).

Table 2. $\delta^{13}C$ and $\delta^{18}O$ values for modern carbonates sampled in the Bagua basin.

Sample	$\delta^{13}C$‰ (VPDB)	$\delta^{18}O$‰ (VPDB)	$\delta 18O_{mw}$‰ (VSMOW)	$\delta 13C_o$‰ (VPDB)	Type
16BG40c	−8.4	−5.5	−3.2	−23.0	Pedogenic carbonate
14BB52C	−8.9	−4.2	−1.9	−23.5	Snail carbonate shell
14BB01CB	−11.1	−4.2	−1.9	−25.8	Snail carbonate shell

Analytical errors 1 sigma on $\delta^{18}O$ = ±0.1 and $\delta^{13}C$ = ±0.06.

The carbon isotopic composition of modern plants yielded a mean $\delta^{13}C_o$ value of ~−28‰ for shrubs and ~−13‰ for grasses (Table 3). The carbon isotopic composition from pedogenic carbonate nodules recovered from a modern-Holocene soil yielded a $\delta^{13}C_{pc}$ value of −8.4‰ (Table 2). The carbon isotopic composition of soil-respired CO_2 calculated from this value yields a $\delta^{13}C$ of −23‰.

Table 3. $\delta^{13}C_o$ values for modern plants samples in the Bagua Basin.

Sample	$\delta^{13}C$‰ (VPDB)	Type
16BG10p	−30.2	Bush
16BG03p	−29.5	Bush
16BG01p	−28.3	Bush
16BG02p	−27.1	Bush
16BG11p	−26.9	Bush
16BG12p	−25.8	Bush
16BG06p	−13.8	Grass
16BG08p	−13.5	Grass
16BG14p	−12.8	Grass
Arithmetic mean	−23.1	-

4.2. Fundo El Triunfo and Sambimera Formations $\delta^{18}O$ and $\delta^{13}C$

The $\delta^{18}O_{mw}$ values reconstructed from pedogenic carbonates collected from paleosols of the Fundo El Triunfo Formation yielded a mean $\delta^{18}O$ value of −2.7‰ ± 0.7 (Figure 2 and Table 4). Oxygen isotopic composition of meteoric water reconstructed from pedogenic carbonates collected from paleosols of the Sambimera Formation yielded a mean $\delta^{18}O$ value of −4.6‰ ± 0.8 (Figure 2 and Table 4).

Pedogenic carbonates from paleosols of the Fundo El Triunfo and Sambimera formations show mean $\delta^{13}C_{pc}$ values of −11.3‰ and −11.2‰ respectively (Figure 2 and Table 4). The carbon isotopic composition of soil-respired CO_2 was reconstructed considering a fractionation of −9.7‰ between soil CO_2 and calcite during pedogenic carbonate precipitation together with a fractionation of −4.4‰ of soil CO_2 through diffusion to the atmosphere [63]. Carbon isotopic composition of soil-respired CO_2 yielded $\delta^{13}C$ means of −25.3‰ and −25.2‰ for the Fundo El Triunfo and the Sambimera formations, respectively.

Table 4. $\delta^{13}C$ and $\delta^{18}O$ values for the pedogenic carbonates samples from the Fundo El Triunfo and Sambimera formations.

Formation	Strat Meter	Sample	$\delta^{13}C_{pc}$‰ (VPDB)	$\delta^{18}O_{pc}$‰ (VPDB)	$\delta^{18}O_{mw}$‰ (VSMOW)	$\delta^{13}C_o$‰ (VPDB)
Fundo El Triunfo Fm	7	14FT32c	−10.8	−6.9	−3.6	−24.7
	8	14FT35c	−9.7	−6.9	−3.6	−23.7
	9	14FT53c	−10.1	−6.1	−2.8	−24.0
	12	14FT08c	−11.8	−5.6	−2.3	−25.7
	15	14FT12c	−12.4	−6.4	−3.1	−26.3
	16	14FT14c	−11.2	−5.8	−2.5	−25.1
	17	14FT15c	−11.1	−5.5	−2.2	−25.0
	32	15BB45c	−12.5	−5.8	−2.5	−26.5
	55	15BB47c	−12.4	−4.7	−1.4	−26.3

Table 4. *Cont.*

Formation	Strat Meter	Sample	$\delta^{13}C_{pc}$‰ (VPDB)	$\delta^{18}O_{pc}$‰ (VPDB)	$\delta^{18}O_{mw}$‰ (VSMOW)	$\delta^{13}C_{o}$‰ (VPDB)
Lower Sambimera Fm	678	15BB58c	−10.2	−8.5	−5.3	−24.1
	850	14SM41c	−10.2	−9.0	−5.7	−24.1
	851	14SM43c	−10.4	−8.8	−5.6	−24.3
	855	14SM47c	−10.2	−9.4	−6.1	−24.2
	900	15BB75c	−8.4	−7.8	−4.5	−22.4
	1073	16BG09c	−11.4	−8.4	−5.1	−25.4
	1075	16BG08c	−11.2	−8.4	−5.1	−25.1
	1085	16BG10c	−10.9	−7.7	−4.4	−24.8
	1089	16BG11c	−11.2	−7.5	−4.2	−25.1
	1255	14SM22c	−10.5	−8.5	−5.2	−24.4
	1275	16BG14c	−10.9	−8.1	−4.8	−24.8
	1370	15BB71c	−12.2	−7.1	−3.8	−26.2
	1578	16BG21c	−10.9	−7.9	−4.6	−24.8
	1666	16BG24c	−10.8	−7.0	−3.7	−24.8
Upper Sambimera Fm	1868	15BB01c	−11.9	−7.7	−4.4	−25.8
	1880	15BB06c	−9.0	−9.3	−6.0	−23.0
	1897	15BB08c	−12.0	−7.4	−4.2	−25.9
	1922	15BB10c	−13.0	−7.2	−3.9	−27.0
	1947	15BB17c	−13.1	−6.7	−3.4	−27.0
	2007	15BB16c	−11.6	−7.8	−4.5	−25.6
	2027	15BB15c	−11.6	−7.2	−3.9	−25.6
	2044	15BB14c	−12.3	−8.1	−4.8	−26.2
	2050	15BB24c	−11.0	−10.2	−7.0	−25.0
	2064	15BB28c	−11.7	−7.3	−4.1	−25.7
	2082	15BB27c	−11.3	−7.8	−4.5	−25.2
	2101	15BB31c	−13.9	−6.7	−3.4	−27.8
	2140	15BB32c	−11.3	−7.1	−3.8	−25.2
	2164	15BB37c	−10.6	−7.2	−3.9	−24.6
	2169	16BG30c	−12.1	−7.3	−4.0	−26.0
	2175	16BG31c	−11.0	−8.9	−5.6	−25.0
	2235	16BG37C	−10.8	−7.9	−4.6	−24.7
	2250	14SM20c	−11.5	−8.2	−4.9	−25.4

Analytical errors (1 sigma) on $\delta^{18}O = \pm 0.1$ and $\delta^{13}C = \pm 0.06$.

5. Interpretation

5.1. Modern $\delta^{18}O$ and $\delta^{13}C$

The trend toward more negative $\delta^{18}O_{mw}$ values from rivers and creeks from the Subandean zone, to the Bagua Basin, and to the eastern slope of the Western Cordillera, reflects the rain-shadow effect exerted by the Eastern Cordillera, which receives the more enriched rainfall on its eastern slope, while the Bagua Basin and the eastern slope of the Western Cordillera show the more depleted rainfall (Figure 6 and Table 1).

The meteoric water lines constructed for the Eastern Cordillera and for the Bagua Basin-eastern slope of the Western Cordillera have slopes of 7.26 and 6.54, respectively (Figure 6). The different slopes between these two meteoric water lines are the result of the contrasting climatic conditions between these regions resulting from the Eastern Cordillera as a barrier for the westward traveling Atlantic moisture. While the slope of ~8 for the meteoric water line for the Eastern Cordillera suggests high humidity conditions during rainfall events, the lower slope of the Bagua Basin eastern slope of the Western Cordillera likely reflects drier conditions and non-equilibrium evaporation of rainfall and surface waters [53,74]. One sample of water collected during a rainfall event in the dry season showed oxygen and hydrogen isotopic compositions of −1.1‰ and 9.0‰, respectively. This result suggests strong evaporation during dry season precipitation due to low humidity, highlighting the aridity of this region (Table 1).

$\delta^{18}O$ values obtained from modern pedogenic carbonates and modern snail shells are significantly more positive than $\delta^{18}O_{mw}$ values from small creeks in the basin. This suggests strong evaporation of soil and surface water in the basin during the long dry season.

The $\delta^{13}C$ values obtained from modern plants and modern pedogenic carbonates reflect the floristic composition of the prevailing biome in the Bagua Basin, which is comprised of a mix of C3 shrubs and some C4 grasses.

5.2. Fundo El Triunfo and Sambimera Formations $\delta^{18}O$ and $\delta^{13}C$

Oxygen isotopic composition of meteoric water reconstructed from pedogenic carbonates collected from paleosols of the Campanian Fundo El Triunfo Formation suggest that these paleosols were formed in an environment relatively proximal to the source of moisture where the water vapor had not experienced significant ^{18}O depletion prior to precipitation. The $\delta^{18}O_{mw}$ values reconstructed from pedogenic carbonates collected from paleosols of the uppermost Eocene–middle Miocene Sambimera Formation suggest a more distal environment of deposition (relative to the source of moisture) compared to Fundo El Triunfo Formation. However, when compared with the oxygen isotopic composition of modern meteoric water of the Bagua Basin, the Sambimera Formation received less depleted precipitation, with $\delta^{18}O_{mw}$ values more positive by ~3‰.

Pedogenic carbonates from paleosols of the Fundo El Triunfo and Sambimera formations $\delta^{13}C_{pc}$ values suggest that from the Campanian and up to the middle Miocene, the floristic landscape of the Bagua Basin was dominated by C3 trees and shrubs with open to semi-open canopy.

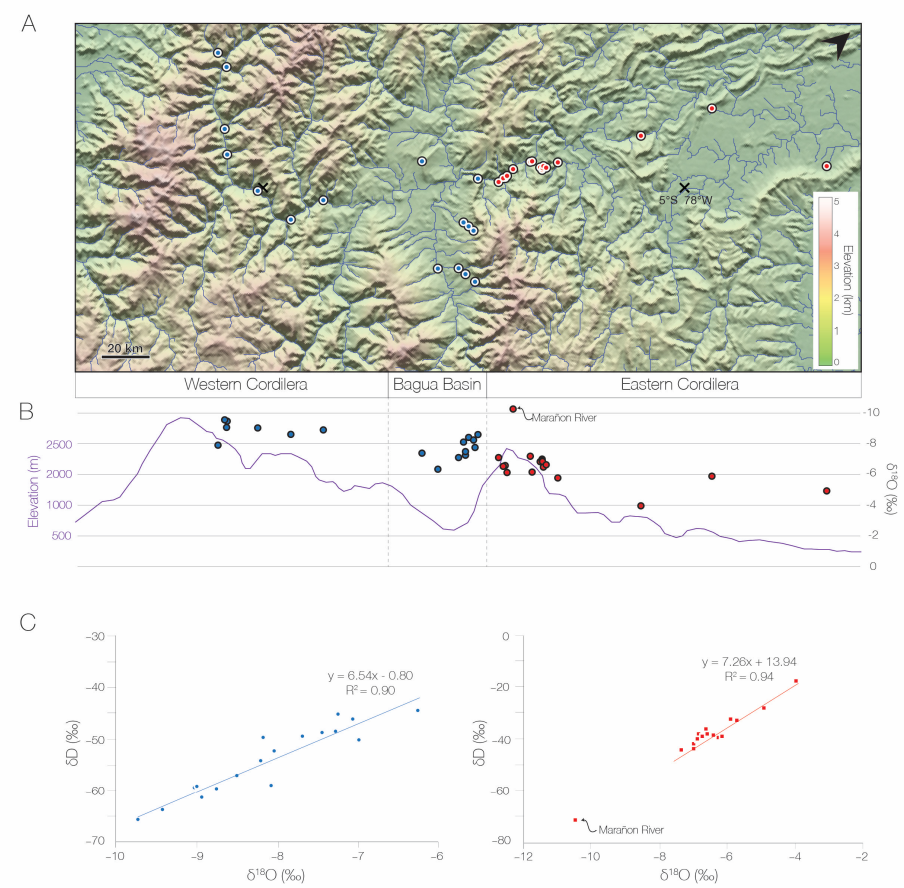

Figure 6. (**A**) Digital elevation model of the Bagua Basin and neighboring Western and Eastern cordilleras showing the location of meteoric water samples (blue and red dots). (**B**) Swath topographic profile across the area depicted in panel (**A**), showing the $\delta^{18}O$ values for the meteoric water samples

analyzed along with their location along the transect. (**C**) Meteoric water lines plotted for the meteoric water samples from the eastern slope of the Eastern Cordillera and Subandean zone (red) and from the Bagua Basin and eastern slope of the Western Cordillera (blue). One sample collected from the Marañon River (labeled on figure) is not considered in the meteoric water line slope calculation.

6. Discussion: Paleogeography of the Northernmost Central Andes

During the Campanian, the Fundo El Triunfo Formation was deposited in a meandering fluvial system in the distal foredeep of a foreland basin associated with a juvenile Andean orogen [25]. Coeval sedimentary units from neighboring basins in the east were deposited in shallow marine environments, revealing the existence of an epicontinental sea in the western Amazon basin during the latest Cretaceous [75,76]. Oxygen isotopic composition of meteoric water reconstructed from pedogenic carbonates from paleosols in the Fundo El Triunfo Formation exhibit relatively enriched values, suggesting a proximal moisture source. We suggest that the eastern epicontinental sea was the primary moisture source for the precipitation falling in Bagua Basin during the Campanian (Figure 2).

The more depleted oxygen isotopic composition reconstructed from the uppermost Eocene-middle Miocene Sambimera Formation suggest the retreat of the epicontinental sea, and the deposition of this unit in an inland environment that has been described as a meandering to braided fluvial system in the proximal foredeep and wedge-top settings of a foreland basin coupled with the Andean orogen (Figure 2) [25]. Interestingly, the oxygen isotopic composition of meteoric water from small rivers and creeks in the modern wedge-top Subandean zone is similar to that reconstructed from the Sambimera Formation pedogenic carbonates, suggesting similar environmental conditions. When compared to modern $\delta^{18}O_{mw}$ values from small rivers and creeks in the Bagua Basin, the $\delta^{18}O_{mw}$ values reconstructed from pedogenic carbonates from the Sambimera Formation are significantly more positive, suggesting that until the middle Miocene the precipitation in Bagua Basin was less depleted in ^{18}O compared to modern times.

The carbon isotopic composition of plants and soil-respired CO_2 reconstructed from pedogenic carbonates from the Fundo El Triunfo and Sambimera formations are significantly more negative than modern values obtained from a modern-Holocene soil and modern plants collected in the basin. This difference partially reflects the late Miocene global expansion of C4 plants [67], but may also reflect the more arid conditions that prevail today. These more arid conditions, favorable for C4 plants, are likely the result of the uplift of the Eastern Cordillera and generation of a rain-shadow in the Bagua Basin.

Together, these results suggest that the uplift of the Eastern Cordillera took place after deposition of the Sambimera Formation, as it is the main factor controlling the increased distillation of the precipitation falling in the Bagua Basin today. This interpretation is in line with previous studies conducted on the Bagua Basin and in the northern Central Andes. Thermochronological analysis ~150 km south of Bagua Basin bracket was carried out on the initial exhumation of the Eastern Cordillera to the middle to late Miocene [7]. Additionally, detrital zircon provenance analysis conducted in the Cenozoic units of the Bagua Basin revealed contrasting detrital zircon age spectra between the Sambimera and the overlying San Antonio formations [25]. The detrital zircon age spectra from the Sambimera Formation is dominated by syn-depositional zircons derived from an active volcanic arc and by Paleozoic zircons derived from the metamorphic basement, which crops out in the Western Cordillera. Conversely, the San Antonio Formation detrital zircon age spectra suggest recycling of zircons from underlying Cenozoic units that are uplifted and eroded in the Eastern Cordillera domain [25]. Stable isotopes analyses in this study together with previous studies of sedimentary provenance suggest that the Eastern Cordillera became a topographic high after deposition of the Sambimera Formation. Unfortunately, due to a lack of pedogenic carbonates in younger formations, our record does not resolve whether modern elevations were achieved during the late Miocene, while the San Antonio Formation was deposited, or later during Pliocene–Pleistocene times.

7. Potential Drivers of the Contrasting Elevation Histories of the Northernmost Central Andes and the Central Andean Plateau

Crustal shortening and associated thickening may result in the removal of mantle lithosphere and/or lower crustal flow that drive punctuated episodes of surface uplift [77–80]. These processes have been used to explain the modern topography of large high-elevation, low-relief plateaus such as the Colorado Plateau, the Tibetan Plateau, and the Central Andean Plateau [70,81–88]. The modern crustal thickness of the Central Andes has been studied through seismic imaging and density models [89,90]. These studies show changes in crustal thickness between the relatively wide Central Andean Plateau (crustal thickness ~70 km) and underneath the narrow northernmost Central Andes (crustal thickness ~40 km). If a critical crustal thickness is required to trigger middle–lower crust flow and removal of mantle lithosphere, then the shortening histories of mountain belts are important for understanding contrasting elevation histories within an orogen.

Along-strike differences in total shortening can be then considered the primary factor controlling the contrasting crustal thickness and elevation between the Central Andean Plateau and the northernmost Central Andes. Several factors may influence shortening magnitude including plate velocity, subduction angle, and precipitation regimes [1–4]. Below we present a short review on the shortening estimates of the Central Andean Plateau and the northernmost Central Andes. Then, we discuss the historical contrasts between first-order factors controlling shortening magnitudes in both regions.

7.1. Shortening Estimates

The shortening history in the Central Andean Plateau has been studied through structural geology and thermochronology modeling. The estimates of shortening at these latitudes vary from ~200 km up to ~350 km [9,91–98] and correspond to up to 40% shortening [9,98].

Shortening in the northern Central Andes spanning the Eastern Cordillera and Subandean zone has been estimated based on a 500-km-long structural cross section located ~150 km south of the Bagua Basin [7]. Other studies have calculated shortening amount in the Subandean zone [24,29,99,100], Bagua Basin [101], and Marañon Fold-Thrust belt [102]. Eude, et al. (2015) [7] calculated 142 km (equivalent to 28%) of shortening in their balanced cross section spanning the Eastern Cordillera and Subandean zone. The shortening estimates for the Sub-Andean Zone of the northern Central Andes vary from 11 km in the Santiago Basin (equivalent to 13.5%) to 101 km (equivalent to 51%) in the Pachitea Basin [99], 70 km in the Huallaga Basin (equivalent to ~14%), and 76 km in the Moyabamba Basin (equivalent to ~12%) [29]. Baca Alvarez (2014) calculated 47 km (equivalent to 38%) of shortening for the Bagua Basin, which is located in the Eastern Cordillera morphotectonic province. Scherrenberg, et al. (2014) [102] calculated shortening amounts in the Marañon Fold-Thrust belt ranging from 22 to 32 km (equivalent to 27% to 41% respectively). The large differences in shortening between basin scale sections can be explained by stratigraphic variations, such as the presence or absence of good detachment levels, and/or the role of inherited structures, such as the Cenozoic reactivation of the Mesozoic rift in the Bagua Basin.

Combining shortening estimates for the adjacent morphotectonic provinces (i.e., Marañon Fold-Thrust belt, Eastern Cordillera, and Sub-Andean zone), the greatest minimum-estimated shortening for the northern Central Andes is ~174 km (Figure 7). Critically, this suggests that the total amount of shortening in the Central Andean Plateau exceeds that of the northern Central Andes by up to 175 km, consistent with twice as much shortening in the Central Andean Plateau. Furthermore, combined shortening estimates for the Bagua and Santiago basins, located at similar latitudes, account for only 58 km. Adding this shortening to the maximum shortening calculated in the Marañon Fold-Thrust belt of 32 km amounts to only 90 km of shortening in this northernmost segment of the Central Andes with lowest topographic expression (Figure 7).

7.2. Overriding Plate Velocity

The last 170 million years of velocity of the South American plate has been investigated using kinematic global plate tectonic models along with geological records preserved in the continental crust [103,104]. The velocity of the overriding plate is a driving mechanism for plate coupling that varies in time and that ultimately controls the tectonic regime. However, plate convergence angle and rates have low variability along a given plate boundary, and so they might have little influence on coeval, along strike variations in the morphotectonic configuration of the margin itself [103]. Indeed, trench normal, absolute velocities of the South American plate during the Late Cretaceous and Cenozoic are fairly similar for the northernmost Central Andes and the Central Andean Plateau [104] (Figure 7), being characterized by positive values that are in line with the overall contractional Andean regime.

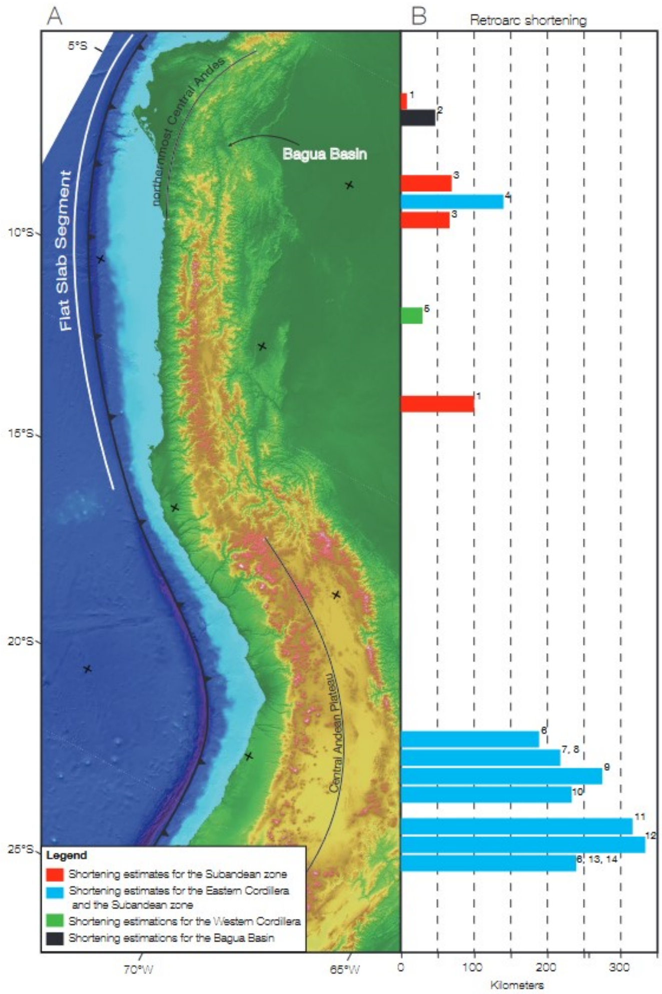

Figure 7. (**A**) Digital elevation model of the Central Andes and relevant morphotectonic features. (**B**) Retro-arc shortening estimations for the Central Andes, adapted from Horton (2018) [103]. References in figure are: (1) Gil Rodriguez et al., (2001) [99], (2) Baca Alvarez (2004) [101], (3) Calderon et al., (2017) [29], (4) Eude et al., (2015) [7], (5) Scherrenberg et al., (2014) [102], (6) Baby et al., (1997) [93], (7) Roeder (1988) [94], (8) Roeder and Chamberlain (1995) [95], (9) McQuarrie et al., (2008) [9], (10) Sheffels (1990) [97], (11) McQuarrie (2002) [96], (12) Anderson et al., (2017) [98], (13) Kley (1996) [91], and (14) Kley et al., (1997) [92]. Blue bars represent shortening estimates of combined Eastern Cordillera and Subandean zone; red bars represent shortening estimates for only the Subandean zone; green bars represent shortening estimations for the Western Cordillera (i.e., Marañon fold-thrust belt); and black bars represent shortening estimation for the Bagua Basin.

7.3. Subduction Angle: Slab Dip

Slab dip exerts significant control on the tectonic regime, regulating the degree of magmatic addition, interplate coupling, and hence, rates of shortening [103,105]. Shallower slab dips promote interplate coupling and contractional tectonic regimes. Steeper slab dips result in lower interplate coupling, allowing for slab rollback and extensional tectonics regimes [103]. The slab dip history in a plate boundary can be reconstructed by tracing the magmatic arc extent at different times and/or using seismic tomography [1,105–108]. The Late Cretaceous through Cenozoic slab dip histories of the northernmost Central Andes and Central Andean Plateau are marked by diachronous episodes of flat slab subduction (Figure 8). Cessation of magmatic activity and increased deformation and crustal thickening in the Eastern Cordillera record a middle Eocene–early Miocene flat slab subduction episode in the Central Andean Plateau [1,109,110]. Crustal thickness estimates suggest significant increases across this period [19]. In contrast, during this time frame, the northernmost Central Andes experienced extensive magmatic activity, suggesting normal subduction [25]. A period of reduced volcanism spanning the late Cretaceous to early Eocene was reported for the northernmost Central Andes, although this episode does not seem to coexist either with a major advance in the deformation front or with increased rates of shortening [25]. Whether this episode corresponds with a flat slab subduction event remains elusive. Flat slab subduction in the northernmost segment of the Central Andes started sometime in the late Miocene and has been associated with the subduction of the Inca lost plateau and the Nazca Ridge (Figure 8) [105,111–113]. The late Miocene–Pliocene in the northernmost Central Andes is characterized by the propagation of the deformation front to the east, resulting in increasing shortening rates in the Eastern Cordillera and Sub-Andean domains [7,24,25,29]. Large shortening rates and earlier crustal thickening in the Central Andean Plateau documented for the middle Eocene–early Miocene [9,114] correspond with a protracted phase of flat slab subduction in that region. In contrast, flat slab subduction and increased shortening rates have only been active since ca. 15–11 Ma in northernmost Central Andes (e.g., Rosenbaum et al., 2005; Hampel et al., 2002), which has not yet driven large crustal thickening. In this manner, the differing slab dip histories and, in particular, the diachronous passage of the flat slab subduction episodes in the Central Andean Plateau and the northernmost Central Andes, might be largely responsible for the contrasting topographic configuration between both of these Andean segments.

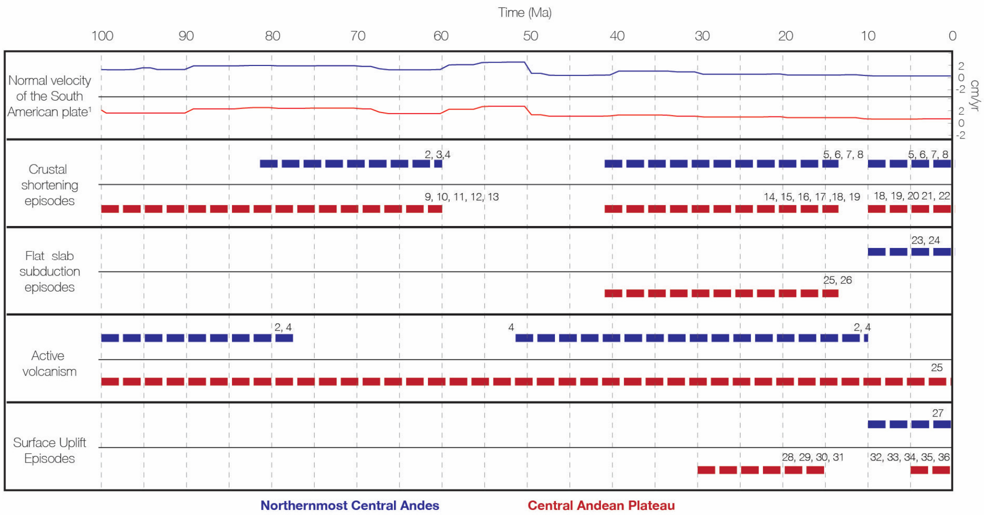

Figure 8. Comparison of the tectonic history and major orogenic events between the Central Andean Plateau (red) and the northernmost Central Andes (blue). References in figure are: (1) Maloney et al., (2013) [104], (2) George et al., (2019) [11], (3) Mégard (1984) [13], (4) Moreno et al., (2020) [25], (5) Eude et al.,

(2015) [7], (6) Hermoza et al., (2005) [24], (7) Calderon et al., (2017) [29], (8) Scherrenberg et al., (2014) [102], (9) Arriagada et al., (2006) [14], (10) Díaz (1977) [16], (11) Haschke and Gunther (2003) [17], (12) Mpodozis et al., (2005) [15], (13) Scheuber and Reutter (1992) [18], (14) Coutand et al., (2001) [20], (15) DeCelles et al., (2011) [22], (16) DeCelles and Horton (2003) [21], (17) Gillis et al., (2006) [23], (18) McQuarrie et al., (2008) [9], (19) McQuarrie et al., (2005) [10], (20) Echavarria et al., (2003) [26], (21) Lease et al., (2016) [28], (22) Uba et al., (2009) [27], (23) Gutscher et al., (1999) [111], (24) Gutscher et al., (2000) [105], (25) James and Sacks (1999) [109], (26) Ramos and Folguera (2009) [1], (27) this work, (28) Garzione et al., (2014) [32], (29) Leier et al., (2013) [31], (30) Saylor and Horton (2014) [30], (31) Sundell et al., (2019) [6], (32) Bershaw et al., (2010) [33], (33) Garzione et al., (2006) [34], (34) Ghosh et al., (2006) [35], (35) Graham et al., (2001) [37], and (36) Kar et al., (2016) [36].

7.4. Precipitation Regimes

Precipitation-induced erosion is a first-order factor controlling exhumation and shortening rates in orogenic belts [115,116]. According to critical wedge theory, as erosion reduces the taper of the wedge, internal shortening provides a mechanism to rebuild the taper [117–119]. Since at least middle Miocene, precipitation in the Central Andes has been characterized by strong orographic rainfall in the eastern slope of the Andean belt [56,71,120,121]. Paleoclimate simulations for times when the Andes were 50% of their modern elevation predict precipitation rates for the latitudes of the Central Andean Plateau that are higher than those of the northernmost Central Andes [54,121]. The main driver for changes in the precipitation regime predicted by paleoclimatic simulations is the elevation gain in the Andean belt. According to the elevation history of the Central Andes previously discussed, the Central Andean Plateau formed an orographic barrier since early Miocene time, promoting large orographic rainfall rates on the lee side of the range that, in turn, induced erosion, ultimately driving internal shortening in the orogenic wedge. A less-intense precipitation regime in the lower northernmost Central Andes associated with minimal erosion might have enabled the eastward propagation of the deformation front without major internal shortening in the orogen. These potential differences in the Neogene precipitation regimes of the Central Andean Plateau and the northernmost Central Andes may have contributed to the contrasting shortening history between the two regions.

8. Conclusions

During Campanian–Paleocene times, the environmental conditions of the Bagua Basin were characterized by a C3-dominated biome in a near-coastal setting along an epicontinental sea. By the late Eocene, the environment evolved to more interior conditions with the prevalence of a C3 vegetation. Such conditions persisted in the basin up until at least the middle Miocene. Sometime after ~13 Ma, the Eastern Cordillera developed as an orographic barrier for the moist air traveling westward from the Atlantic Ocean, driving a shift to drier environmental conditions in the newly formed intermontane basin. At present, the Bagua Basin is characterized by a C3–C4 mixed biome in a dry, intermontane setting.

New stable isotope results shed light on the elevation history of the Eastern Cordillera. Stable isotopes results in this study suggest the establishment of the Eastern Cordillera as an orographic barrier for the moist low-level Amazonian jet sometime after ~13 Ma. U-Pb zircon provenance analysis from the Sambimera and San Antonio formations [25] reveals the establishment of the Eastern Cordillera as a drainage divide beginning as early as the middle Miocene (i.e., ~11 Ma), but the precise timing of the establishment of the current relief of Eastern Cordillera orographic barrier remains unresolved.

We suggest that the contrasting topographic expression and crustal thickness of the northernmost Central Andes and the Central Andean Plateau is the result of the differences in the shortening history of these two Central Andean segments. The diachroneity of flat slab subduction episodes is inferred to be the major factor responsible for their different shortening histories. While the Central Andean Plateau reached its peak rates of shortening during the middle Eocene–early Miocene flat slab subduction episode, the northernmost

Central Andes only started experiencing flat slab subduction in the late Miocene and its shortening rates have increased since then. The northernmost Central Andes, therefore, serve as a potential analogue for a juvenile Central Andean Plateau, with the intermontane Bagua Basin as the equivalent of the Altiplano Basin before it was uplifted to its high elevation position.

Author Contributions: Conceptualization, F.M. and C.N.G.; Data curation, F.M. and L.W.; Formal analysis, F.M.; Funding acquisition, C.N.G.; Investigation, F.M., C.N.G., S.W.M.G., L.W., F.R. and A.B.; Methodology, F.M. and C.N.G.; Visualization, F.M. and L.W.; Writing—original draft, F.M.; Writing—review & editing, C.N.G. and S.W.M.G. All authors have read and agreed to the published version of the manuscript.

Funding: This research was funded by the University of Rochester and the National Science Foundation (EAR 1338694).

Data Availability Statement: All the data produced and analyzed in this work are available in the tables and figures of this paper.

Acknowledgments: The authors thank Pennilyn Higgins for her assistance in the data acquisition. This article benefited from insightful conversations and feedback from Gautam Mitra, Lin Li, Carlie Mentzer, and anonymous reviewers.

Conflicts of Interest: The authors declare no conflict of interest.

References

1. Ramos, V.A.; Folguera, A. Andean flat-slab subduction through time. *Geol. Soc. Lond. Spec. Publ.* **2009**, *327*, 31–54. [CrossRef]
2. Pardo-Casas, F.; Molnar, P. Relative motion of the Nazca (Farallon) and South American Plates since Late Cretaceous time. *Tectonics* **1987**, *6*, 233–248. [CrossRef]
3. Haschke, M.R.; Scheuber, E.; Gunther, A.; Reutter, K.-J. Evolutionary cycles during the Andean orogeny: Repeated slab breakoff and flat subduction? *Terra Nova* **2002**, *14*, 49–55. [CrossRef]
4. Strecker, M.; Alonso, R.; Bookhagen, B.; Carrapa, B.; Hilley, G.; Sobel, E.; Trauth, M. Tectonics and Climate of the Southern Central Andes. *Annu. Rev. Earth Planet. Sci.* **2007**, *35*, 747–787. [CrossRef]
5. Garzione, C.N.; McQuarrie, N.; Perez, N.D.; Ehlers, T.A.; Beck, S.L.; Kar, N.; Eichelberger, N.; Chapman, A.D.; Ward, K.M.; Ducea, M.N.; et al. Tectonic Evolution of the Central Andean Plateau and Implications for the Growth of Plateaus. *Annu. Rev. Earth Planet. Sci.* **2017**, *45*, 529–559. [CrossRef]
6. Sundell, K.E.; Saylor, J.; Lapen, T.J.; Horton, B.K. Implications of variable late Cenozoic surface uplift across the Peruvian central Andes. *Sci. Rep.* **2019**, *9*, 4877. [CrossRef]
7. Eude, A.; Roddaz, M.; Brichau, S.; Brusset, S.; Calderon, Y.; Baby, P.; Soula, J.-C. Controls on timing of exhumation and deformation in the northern Peruvian eastern Andean wedge as inferred from low-temperature thermochronology and balanced cross section. *Tectonics* **2015**, *34*, 715–730. [CrossRef]
8. Scherrenberg, A.F.; Kohn, B.P.; Holcombe, R.J.; Rosenbaum, G. Thermotectonic history of the Marañón Fold–Thrust Belt, Peru: Insights into mineralisation in an evolving orogen. *Tectonophysics* **2016**, *667*, 16–36. [CrossRef]
9. McQuarrie, N.; Barnes, J.; Ehlers, T.A. Geometric, kinematic, and erosional history of the central Andean Plateau, Bolivia (15–17° S). *Tectonics* **2008**, *27*, 0278–7407. [CrossRef]
10. McQuarrie, N.; Horton, B.K.; Zandt, G.; Beck, S.; DeCelles, P.G. Lithospheric evolution of the Andean fold–thrust belt, Bolivia, and the origin of the central Andean plateau. *Tectonophysics* **2005**, *399*, 15–37. [CrossRef]
11. George, S.W.; Horton, B.K.; Jackson, L.J.; Moreno, F.; Carlotto, V.; Garzione, C.N. Sediment provenance variations during contrasting Mesozoic-early Cenozoic tectonic regimes of the northern Peruvian Andes and Santiago-Marañón foreland basin. In *Andean Tectonics*; Horton, B.K., Folguera, A., Eds.; Elsevier: Amsterdam, The Netherlands, 2019; pp. 269–296. [CrossRef]
12. Horton, B. Sedimentary record of Andean mountain building. *Earth-Sci. Rev.* **2018**, *178*, 279–309. [CrossRef]
13. Mégard, F. The Andean orogenic period and its major structures in central and northern Peru. *J. Geol. Soc.* **1984**, *141*, 893–900. [CrossRef]
14. Arriagada, C.; Cobbold, P.R.; Roperch, P. Salar de Atacama basin: A record of compressional tectonics in the central Andes since the mid-Cretaceous. *Tectonics* **2006**, *25*, 1–19. [CrossRef]
15. Mpodozis, C.; Arriagada, C.; Basso, M.; Roperch, P.; Cobbold, P.; Reich, M. Late Mesozoic to Paleogene stratigraphy of the Salar de Atacama Basin, Antofagasta, Northern Chile: Implications for the tectonic evolution of the Central Andes. *Tectonophysics* **2005**, *399*, 125–154. [CrossRef]
16. Díaz, G.C. Contribution to the knowledge of the Domeyko Range in the Andes of Northern Chile. *Geol. Rundsch.* **1977**, *66*, 374–404. [CrossRef]

17. Haschke, M.; Günther, A. Balancing crustal thickening in arcs by tectonic vs. magmatic means. *Geology* **2003**, *31*, 933–936. [CrossRef]
18. Scheuber, E.; Reutter, K.-J. Magmatic arc tectonics in the Central Andes between 21° and 25° S. *Tectonophysics* **1992**, *205*, 127–140. [CrossRef]
19. Sundell, K.E.; George, S.W.; Carrapa, B.; Gehrels, G.E.; Ducea, M.N.; Saylor, J.E.; Pepper, M. Crustal Thickening of the Northern Central Andean Plateau Inferred from Trace Elements in Zircon. *Geophys. Res. Lett.* **2022**, *49*, e2021GL096443. [CrossRef]
20. Coutand, I.; Cobbold, P.R.; De Urreiztieta, M.; Gautier, P.; Chauvin, A.; Gapais, D.; Rossello, E.A.; López-Gamundí, O. Style and history of Andean deformation, Puna plateau, northwestern Argentina. *Tectonics* **2001**, *20*, 210–234. [CrossRef]
21. DeCelles, P.G.; Horton, B.K. Early to middle Tertiary foreland basin development and the history of Andean crustal shortening in Bolivia. *GSA Bull.* **2003**, *115*, 58–77. [CrossRef]
22. DeCelles, P.G.; Carrapa, B.; Horton, B.K.; E Gehrels, G. Cenozoic foreland basin system in the central Andes of northwestern Argentina: Implications for Andean geodynamics and modes of deformation. *Tectonics* **2011**, 1–30. [CrossRef]
23. Gillis, R.J.; Horton, B.K.; Grove, M. Thermochronology, geochronology, and upper crustal structure of the Cordillera Real: Implications for Cenozoic exhumation of the central Andean plateau. *Tectonics* **2006**, *25*. [CrossRef]
24. Hermoza, W.; Brusset, S.; Baby, P.; Gil, W.; Roddaz, M.; Guerrero, N.; Bolaños, R. The Huallaga foreland basin evolution: Thrust propagation in a deltaic environment, northern Peruvian Andes. *J. S. Am. Earth Sci.* **2005**, *19*, 21–34. [CrossRef]
25. Moreno, F.; Garzione, C.N.; George, S.W.M.; Horton, B.K.; Williams, L.; Jackson, L.J.; Carlotto, V.; Richter, F.; Bandeian, A. Coupled Andean Growth and Foreland Basin Evolution, Campanian–Cenozoic Bagua Basin, Northern Peru. *Tectonics* **2020**, *39*, e2019TC005967. [CrossRef]
26. Echavarria, L.; Hernández, R.; Allmendinger, R.W.; Reynolds, J. Subandean thrust and fold belt of northwestern Argentina: Geometry and timing of the Andean evolution. *AAPG Bull.* **2003**, *87*, 965–985. [CrossRef]
27. Uba, C.E.; Kley, J.; Strecker, M.R.; Schmitt, A. Unsteady evolution of the Bolivian Subandean thrust belt: The role of enhanced erosion and clastic wedge progradation. *Earth Planet. Sci. Lett.* **2009**, *281*, 134–146. [CrossRef]
28. Lease, R.O.; Ehlers, T.A.; Enkelmann, E. Large along-strike variations in the onset of Subandean exhumation: Implications for Central Andean orogenic growth. *Earth Planet. Sci. Lett.* **2016**, *451*, 62–76. [CrossRef]
29. Calderon, Y.; Baby, P.; Hurtado, C.; Brusset, S. Thrust tectonics in the Andean retro-foreland basin of northern Peru: Permian inheritances and petroleum implications. *Mar. Pet. Geol.* **2017**, *82*, 238–250. [CrossRef]
30. Saylor, J.; Horton, B.K. Nonuniform surface uplift of the Andean plateau revealed by deuterium isotopes in Miocene volcanic glass from southern Peru. *Earth Planet. Sci. Lett.* **2014**, *387*, 120–131. [CrossRef]
31. Leier, A.; McQuarrie, N.; Garzione, C.; Eiler, J. Stable isotope evidence for multiple pulses of rapid surface uplift in the Central Andes, Bolivia. *Earth Planet. Sci. Lett.* **2013**, *371–372*, 49–58. [CrossRef]
32. Garzione, C.N.; Auerbach, D.J.; Smith, J.J.-S.; Rosario, J.J.; Passey, B.; Jordan, T.; Eiler, J.M. Clumped isotope evidence for diachronous surface cooling of the Altiplano and pulsed surface uplift of the Central Andes. *Earth Planet. Sci. Lett.* **2014**, *393*, 173–181. [CrossRef]
33. Bershaw, J.; Garzione, C.N.; Higgins, P.; MacFadden, B.J.; Anaya, F.; Alvarenga, H. Spatial–temporal changes in Andean plateau climate and elevation from stable isotopes of mammal teeth. *Earth Planet. Sci. Lett.* **2010**, *289*, 530–538. [CrossRef]
34. Garzione, C.N.; Molnar, P.; Libarkin, J.C.; MacFadden, B.J. Rapid late Miocene rise of the Bolivian Altiplano: Evidence for removal of mantle lithosphere. *Earth Planet. Sci. Lett.* **2006**, *241*, 543–556. [CrossRef]
35. Ghosh, P.; Garzione, C.N.; Eiler, J.M. Rapid Uplift of the Altiplano Revealed Through ^{13}C-^{18}O Bonds in Paleosol Carbonates. *Science* **2006**, *311*, 511–515. [CrossRef] [PubMed]
36. Kar, N.; Garzione, C.N.; Jaramillo, C.; Shanahan, T.; Carlotto, V.; Pullen, A.; Moreno, F.; Anderson, V.; Moreno, E.; Eiler, J. Rapid regional surface uplift of the northern Altiplano plateau revealed by multiproxy paleoclimate reconstruction. *Earth Planet. Sci. Lett.* **2016**, *447*, 33–47. [CrossRef]
37. Graham, A.; Gregory-Wodzicki, K.M.; Wright, K.L. Studies in Neotropical Paleobotany. XV. A Mio-Pliocene palynoflora from the Eastern Cordillera, Bolivia: Implications for the uplift history of the Central Andes. *Am. J. Bot.* **2001**, *88*, 1545–1557. [CrossRef] [PubMed]
38. Hergarten, S.; Robl, J.; Stüwe, K. Extracting topographic swath profiles across curved geomorphic features. *Earth Surf. Dyn.* **2014**, *2*, 97–104. [CrossRef]
39. Montgomery, D.R.; Balco, G.; Willett, S.D. Climate, tectonics, and the morphology of the Andes. *Geology* **2001**, *29*, 579–582. [CrossRef]
40. Pfiffner, A.; Gonzalez, L. Mesozoic–Cenozoic Evolution of the Western Margin of South America: Case Study of the Peruvian Andes. *Geosciences* **2013**, *3*, 262–310. [CrossRef]
41. Noble, D.C.; McKee, E.H.; Mourier, T.; Mégard, F. Cenozoic stratigraphy, magmatic activity, compressive deformation, and uplift in northern Peru. *Geol. Soc. Am. Bull.* **1990**, *102*, 1105–1113. [CrossRef]
42. Bookhagen, B.; Strecker, M.R. Orographic barriers, high-resolution TRMM rainfall, and relief variations along the eastern Andes. *Geophys. Res. Lett.* **2008**, *35*. [CrossRef]
43. Weather Spark. Available online: https://weatherspark.com/ (accessed on 13 April 2022).
44. Climate Data Climate Data for Cities Worldwide—Climate-Data.Org. Available online: https://en.climate-data.org/ (accessed on 13 April 2022).

45. Särkinen, T.; Iganci, J.R.; Linares-Palomino, R.; Simon, M.F.; E Prado, D. Forgotten forests—Issues and prospects in biome mapping using Seasonally Dry Tropical Forests as a case study. *BMC Ecol.* **2011**, *11*, 27. [CrossRef] [PubMed]
46. Olson, D.M.; Dinerstein, E.; Wikramanayake, E.D.; Burgess, N.D.; Powell, G.V.N.; Underwood, E.C.; D'Amico, J.A.; Itoua, I.; Strand, H.E.; Morrison, J.C.; et al. Terrestrial Ecoregions of the World: A New Map of Life on Earth: A New Global Map of Terrestrial Ecoregions Provides an Innovative Tool for Conserving Biodiversity. *Bioscience* **2001**, *51*, 933–938. [CrossRef]
47. Eva, H.D.; Belward, A.S.; De Miranda, E.E.; Di Bella, C.M.; Gond, V.; Huber, O.; Jones, S.; Sgrenzaroli, M.; Fritz, S. A land cover map of South America. *Glob. Chang. Biol.* **2004**, *10*, 731–744. [CrossRef]
48. Garreaud, R.D. The Andes climate and weather. *Adv. Geosci.* **2009**, *22*, 3–11. [CrossRef]
49. Garreaud, R.; Vuille, M.; Compagnucci, R.; Marengo, J. Present-day South American climate. *Palaeogeogr. Palaeoclim. Palaeoecol.* **2009**, *281*, 180–195. [CrossRef]
50. Bershaw, J.; Saylor, J.; Garzione, C.N.; Leier, A.; Sundell, K.E. Stable isotope variations (δ^{18}O and δD) in modern waters across the Andean Plateau. *Geochim. Cosmochim. Acta* **2016**, *194*, 310–324. [CrossRef]
51. Vuille, M.; Bradley, R.S.; Werner, M.; Healy, R.; Keimig, F. Modeling δ^{18}O in precipitation over the tropical Americas: 1. Interannual variability and climatic controls. *J. Geophys. Res. Earth Surf.* **2003**, *108*, D6. [CrossRef]
52. Craig, H. Isotopic Variations in Meteoric Waters. *Science* **1961**, *133*, 1702–1703. [CrossRef]
53. Rozanski, K.; Araguás-Araguás, L.; Gonfiantini, R. Isotopic Patterns in Modern Global Precipitation. *Clim. Chang. Cont. Isot. Rec.* **2013**, *78*, 1–36. [CrossRef]
54. NInsel, N.; Poulsen, C.; Ehlers, T.A.; Sturm, C. Response of meteoric δ18O to surface uplift — Implications for Cenozoic Andean Plateau growth. *Earth Planet. Sci. Lett.* **2012**, *317–318*, 262–272. [CrossRef]
55. Lenters, J.; Cook, K.H. On the Origin of the Bolivian High and Related Circulation Features of the South American Climate. *J. Atmos. Sci.* **1997**, *54*, 656–678. [CrossRef]
56. Insel, N.; Poulsen, C.J.; Ehlers, T.A. Influence of the Andes Mountains on South American moisture transport, convection, and precipitation. *Clim. Dyn.* **2009**, *35*, 1477–1492. [CrossRef]
57. Ampuero, A.; Stríkis, N.M.; Apaéstegui, J.; Vuille, M.; Novello, V.F.; Espinoza, J.C.; Cruz, F.W.; Vonhof, H.; Mayta, V.C.; Martins, V.T.S.; et al. The Forest Effects on the Isotopic Composition of Rainfall in the Northwestern Amazon Basin. *J. Geophys. Res. Atmos.* **2020**, *125*, e2019JD031445. [CrossRef]
58. Fiorella, R.P.; Poulsen, C.; Zolá, R.S.P.; Jeffery, M.L.; Ehlers, T.A. Modern and long-term evaporation of central Andes surface waters suggests paleo archives underestimate Neogene elevations. *Earth Planet. Sci. Lett.* **2015**, *432*, 59–72. [CrossRef]
59. Gonfiantini, R.; Roche, M.-A.; Olivry, J.-C.; Fontes, J.-C.; Zuppi, G.M. The altitude effect on the isotopic composition of tropical rains. *Chem. Geol.* **2001**, *181*, 147–167. [CrossRef]
60. Chamberlain, C.P.; Poage, M.A. Reconstructing the paleotopography of mountain belts from the isotopic composition of authigenic minerals. *Geology* **2000**, *28*, 115–118. [CrossRef]
61. Quade, J.; Garzione, C.; Eiler, J. Paleoelevation Reconstruction using Pedogenic Carbonates. *Rev. Miner. Geochem.* **2007**, *66*, 53–87. [CrossRef]
62. Garzione, C.N.; Dettman, D.L.; Horton, B.K. Carbonate oxygen isotope paleoaltimetry: Evaluating the effect of diagenesis on paleoelevation estimates for the Tibetan plateau. *Palaeogeogr. Palaeoclimatol. Palaeoecol.* **2004**, *212*, 119–140. [CrossRef]
63. Cerling, T.E.; Quade, J. Stable Carbon and Oxygen Isotopes in Soil Carbonates. *Clim. Chang. Cont. Isot. Rec.* **2013**, *78*, 217–231. [CrossRef]
64. Fox, D.L.; Koch, P.L. Tertiary history of C4 biomass in the Great Plains, USA. *Geology* **2003**, *31*, 809. [CrossRef]
65. Cerling, T.E.; Harris, J.M.; MacFadden, B.J.; Leakey, M.G.; Quade, J.; Eisenmann, V.; Ehleringer, J.R. Global vegetation change through the Miocene/Pliocene boundary. *Nature* **1997**, *389*, 153–158. [CrossRef]
66. Ehleringer, J.R.; Cerling, T.E. C3 and C4 photosynthesis. In *Encyclopedia of Global Environmental Change, The Earth System: Biological and Ecological Dimensions of Global Environmental Change*; Wiley: Chichester, UK, 2002; Volume 2, pp. 186–190.
67. Cerling, T.E.; Wang, Y.; Quade, J. Expansion of C4 ecosystems as an indicator of global ecological change in the late Miocene. *Nature* **1993**, *361*, 344–345. [CrossRef]
68. Sage, R.F. The evolution of C4 photosynthesis. *New Phytol.* **2004**, *161*, 341–370. [CrossRef]
69. Sage, R.F.; Monson, R.K.; Ehleringer, J.R.; Adachi, S.; Pearcy, R.W. Some like it hot: The physiological ecology of C4 plant evolution. *Oecologia* **2018**, *187*, 941–966. [CrossRef]
70. Garzione, C.N.; Hoke, G.D.; Libarkin, J.C.; Withers, S.; MacFadden, B.; Eiler, J.; Ghosh, P.; Mulch, A. Rise of the Andes. *Science* **2008**, *320*, 1304–1307. [CrossRef]
71. Mulch, A.; Uba, C.E.; Strecker, M.R.; Schoenberg, R.; Chamberlain, C.P. Late Miocene climate variability and surface elevation in the central Andes. *Earth Planet. Sci. Lett.* **2010**, *290*, 173–182. [CrossRef]
72. Kim, S.-T.; O'Neil, J.R. Equilibrium and nonequilibrium oxygen isotope effects in synthetic carbonates. *Geochim. Cosmochim. Acta* **1997**, *61*, 3461–3475. [CrossRef]
73. Bottinga, Y. Calculation of fractionation factors for carbon and oxygen isotopic exchange in the system calcite-carbon dioxide-water. *J. Phys. Chem.* **1968**, *72*, 800–808. [CrossRef]
74. Gonfiantini, R. Environmental isotopes in lake studies. In *Handbook of Environmental Isotope Geochemistry, the Terrestrial Environment*; Elsevier: Amsterdam, The Netherlands, 1986; Volume 2, pp. 113–168.

75. Chacaltana, C.A.; Valdivia, W.; Peña, D.F. Estudio geológico de la cuenca Santiago sectores Centro y Sur. *Bol. Ser. D Estud. Reg.* **2012**, *30*, 1607–5617.
76. Hurtado, C.; Roddaz, M.; Santos, R.V.; Baby, P.; Antoine, P.-O.; Dantas, E.L. Cretaceous-early Paleocene drainage shift of Amazonian rivers driven by Equatorial Atlantic Ocean opening and Andean uplift as deduced from the provenance of northern Peruvian sedimentary rocks (Huallaga basin). *Gondwana Res.* **2018**, *63*, 152–168. [CrossRef]
77. Krystopowicz, N.J.; A Currie, C. Crustal eclogitization and lithosphere delamination in orogens. *Earth Planet. Sci. Lett.* **2013**, *361*, 195–207. [CrossRef]
78. Bird, P. Finite element modeling of lithosphere deformation: The Zagros collision orogeny. *Tectonophysics* **1978**, *50*, 307–336. [CrossRef]
79. Kay, R.; Kay, S. Delamination and delamination magmatism. *Tectonophysics* **1993**, *219*, 177–189. [CrossRef]
80. Kay, S.M.; Coira, B.L. Shallowing and steepening subduction zones, continental lithospheric loss, magmatism, and crustalflow under the Central Andean Altiplano-Puna Plateau. In *Backbone of the Americas: Shallow Subduction, Plateau Uplift, and Ridge and Terrane Collision*; The Geological Society of America: Boulder, CO, USA, 2009; Volume 204, p. 229.
81. England, P.; Houseman, G. Extension during continental convergence, with application to the Tibetan Plateau. *J. Geophys. Res. Solid Earth* **1989**, *94*, 17561–17579. [CrossRef]
82. Bird, P. Continental delamination and the Colorado Plateau. *J. Geophys. Res. Earth Surf.* **1979**, *84*, 7561–7571. [CrossRef]
83. Molnar, P.; England, P.; Martinod, J. Mantle dynamics, uplift of the Tibetan Plateau, and the Indian Monsoon. *Rev. Geophys.* **1993**, *31*, 357–396. [CrossRef]
84. Clark, M.K.; Royden, L.H. Topographic ooze: Building the eastern margin of Tibet by lower crustal flow. *Geology* **2000**, *28*, 703–706. [CrossRef]
85. Harrison, T.M.; Copeland, P.; Kidd, W.S.F.; Yin, A.N. Raising Tibet. *Science* **1992**, *255*, 1663–1670. [CrossRef]
86. Sobolev, S.V.; Babeyko, A.Y. What drives orogeny in the Andes? *Geology* **2005**, *33*, 617–620. [CrossRef]
87. Gerbault, M.; Martinod, J.; Hérail, G. Possible orogeny-parallel lower crustal flow and thickening in the Central Andes. *Tectonophysics* **2005**, *399*, 59–72. [CrossRef]
88. Husson, L.; Sempere, T. Thickening the Altiplano crust by gravity-driven crustal channel flow. *Geophys. Res. Lett.* **2003**, *30*. [CrossRef]
89. Beck, S.L.; Zandt, G.; Myers, S.C.; Wallace, T.C.; Silver, P.G.; Drake, L. Crustal-thickness variations in the central Andes. *Geology* **1996**, *24*, 407–410. [CrossRef]
90. Tassara, A.; Götze, H.-J.; Schmidt, S.; Hackney, R. Three-dimensional density model of the Nazca plate and the Andean continental margin. *J. Geophys. Res. Earth Surf.* **2006**, *111*. [CrossRef]
91. Kley, J. Transition from basement-involved to thin-skinned thrusting in the Cordillera Oriental of southern Bolivia. *Tectonics* **1996**, *15*, 763–775. [CrossRef]
92. Kley, J.; Müller, J.; Tawackoli, S.; Jacobshagen, V.; Manutsoglu, E. Pre-Andean and Andean-age deformation in the Eastern Cordillera of southern Bolivia. *J. S. Am. Earth Sci.* **1997**, *10*, 1–19. [CrossRef]
93. Baby, P.; Rochat, P.; Mascle, G.; Hérail, G. Neogene shortening contribution to crustal thickening in the back arc of the Central Andes. *Geology* **1997**, *25*, 883–886. [CrossRef]
94. Roeder, D. Andean-age structure of eastern Cordillera (province of La Paz, Bolivia). *Tectonics* **1988**, *7*, 23–39. [CrossRef]
95. Roeder, D.; Chamberlain, R.L. Structural Geology of Sub-Andean Fold and Thrust Belt in Northwestern Bolivia. In *M 62: Petroleum Basins of South America*; The American Association of Petroleum: Tulsa, OK, USA, 1995. [CrossRef]
96. McQuarrie, N. The kinematic history of the central Andean fold-thrust belt, Bolivia: Implications for building a high plateau. *Geol. Soc. Am. Bull.* **2002**, *114*, 950–963. [CrossRef]
97. Sheffels, B.M. Lower bound on the amount of crustal shortening, in the central Bolivian Andes. *Geology* **1990**, *18*, 812–815. [CrossRef]
98. Anderson, R.B.; Long, S.P.; Horton, B.K.; Calle, A.Z.; Ramirez, V. Shortening and structural architecture of the Andean fold-thrust belt of southern Bolivia (21° S): Implications for kinematic development and crustal thickening of the central Andes. *Geosphere* **2017**, *13*, 538–558. [CrossRef]
99. Gil Rodriguez, W.; Baby, P.; Ballard, J.-F. Structure et contrôle paléogéographique de la zone subandine péruvienne. *C. R. L'Acad. Sci.-Ser. IIA-Earth Planet. Sci.* **2001**, *333*, 741–748. [CrossRef]
100. Aleman, A.M.; Marksteiner, R.X. Structural styles in the Santiago fold and thrust belt, Peru: A salt related orogenic belt. In *Géodynamique Andine: Résumés Étendus = Andean Geodynamics: Extended Abstracts = Geodinamica Andina: Resumenes Expandidos*; Orstom: Paris, France, 1993.
101. Baca Alvarez, M.A. Evolución Tectónica y Sedimentológica Cenozoica de la Cuenca Bagua (Norte del Perú) y sus Implicancias Geodinámicas. Bachelor's Thesis, Universidad Nacional San Antonio del Cusco, Cusco, Peru, 2004.
102. Scherrenberg, A.F.; Holcombe, R.J.; Rosenbaum, G. The persistence and role of basin structures on the 3D architecture of the Marañón Fold-Thrust Belt, Peru. *J. S. Am. Earth Sci.* **2014**, *51*, 45–58. [CrossRef]
103. Horton, B.K. Tectonic Regimes of the Central and Southern Andes: Responses to Variations in Plate Coupling During Subduction. *Tectonics* **2018**, *37*, 402–429. [CrossRef]
104. Maloney, K.T.; Clarke, G.L.; Klepeis, K.A.; Quevedo, L. The Late Jurassic to present evolution of the Andean margin: Drivers and the geological record. *Tectonics* **2013**, *32*, 1049–1065. [CrossRef]

105. Gutscher, M.-A.; Spakman, W.; Bijwaard, H.; Engdahl, E.R. Geodynamics of flat subduction: Seismicity and tomographic constraints from the Andean margin. *Tectonics* **2000**, *19*, 814–833. [CrossRef]
106. Mamani, M.; Worner, G.; Sempere, T. Geochemical variations in igneous rocks of the Central Andean orocline (13 S to 18 S): Tracing crustal thickening and magma generation through time and space. *GSA Bull.* **2009**, *122*, 162–182. [CrossRef]
107. Jordan, T.E.; Isacks, B.L.; Allmendinger, R.W.; Brewer, J.A.; Ramos, V.A.; Ando, C.J. Andean tectonics related to geometry of subducted Nazca plate. *GSA Bull.* **1983**, *94*, 341–361. [CrossRef]
108. Kay, S.; Godoy, E.; Kurtz, A. Episodic arc migration, crustal thickening, subduction erosion, and magmatism in the south-central Andes. *GSA Bull.* **2005**, *117*, 67. [CrossRef]
109. James, D.E.; Sacks, S. Cenozoic formation of the Central Andes: A geophysical perspective. *Soc. Econ. Geol. Spec. Publ.* **1999**, *7*, 1–25.
110. Sandeman, H.A.; Clark, A.H.; Farrar, E. An Integrated Tectono-Magmatic Model for the Evolution of the Southern Peruvian Andes (13–20 °S) since 55 Ma. *Int. Geol. Rev.* **1995**, *37*, 1039–1073. [CrossRef]
111. Gutscher, M.-A.; Olivet, J.-L.; Aslanian, D.; Eissen, J.-P.; Maury, R. The "lost inca plateau": Cause of flat subduction beneath peru? *Earth Planet. Sci. Lett.* **1999**, *171*, 335–341. [CrossRef]
112. Rosenbaum, G.; Giles, D.; Saxon, M.; Betts, P.G.; Weinberg, R.; Duboz, C. Subduction of the Nazca Ridge and the Inca Plateau: Insights into the formation of ore deposits in Peru. *Earth Planet. Sci. Lett.* **2005**, *239*, 18–32. [CrossRef]
113. Hampel, A. The migration history of the Nazca Ridge along the Peruvian active margin: A re-evaluation. *Earth Planet. Sci. Lett.* **2002**, *203*, 665–679. [CrossRef]
114. Müller, J.P.; Kley, J.; Jacobshagen, V. Structure and Cenozoic kinematics of the Eastern Cordillera, southern Bolivia (21 S). *Tectonics* **2002**, *21*, 1-1–1-24. [CrossRef]
115. Willett, S.D. Orogeny and orography: The effects of erosion on the structure of mountain belts. *J. Geophys. Res. Earth Surf.* **1999**, *104*, 28957–28981. [CrossRef]
116. McQuarrie, N.; Ehlers, T.A.; Barnes, J.B.; Meade, B. Temporal variation in climate and tectonic coupling in the central Andes. *Geology* **2008**, *36*, 999. [CrossRef]
117. Davis, D.; Suppe, J.; Dahlen, F.A. Mechanics of fold-and-thrust belts and accretionary wedges. *J. Geophys. Res. Earth Surf.* **1983**, *88*, 1153–1172. [CrossRef]
118. Dahlen, F.A. Critical taper model of fold-and-thrust belts and accretionary wedges. *Annu. Rev. Earth Planet. Sci.* **1990**, *18*, 55–99. [CrossRef]
119. Woodward, N.B. Geological applicability of critical-wedge thrust-belt models. *GSA Bull.* **1987**, *99*, 827. [CrossRef]
120. Rohrmann, A.; Sachse, D.; Mulch, A.; Pingel, H.; Tofelde, S.; Alonso, R.N.; Strecker, M.R. Miocene orographic uplift forces rapid hydrological change in the southern central Andes. *Sci. Rep.* **2016**, *6*, 35678. [CrossRef] [PubMed]
121. Poulsen, C.J.; Ehlers, T.A.; Insel, N. Onset of Convective Rainfall During Gradual Late Miocene Rise of the Central Andes. *Science* **2010**, *328*, 490–493. [CrossRef] [PubMed]